CHAPTER 4

EXTENDED ELASTIC IMPEDANCE (EEI) ANALYSES

4.1 Chi angle determination

To determine the best chi angle (-90° to +90°) at maximum correlation for fluid impedances as study's aims, the cross correlation between EEI curve and target parameter logs were performed. The selected target parameter logs include water saturation (Sw), Vp/Vs ratio, Poisson's Ratio, Bulk modulus, Shear modulus, Lambda-Rho, Mu-Rho, S-wave impedance (Zs), neutron porosity (NPHI), volume of clay (VCL), and Vs^2/Vp^2 or <K> as shown in the followings.

In this study, there are 4 wells to be carried out for best chi angle determination in which the results would not give precisely the same optimum chi angle at all wells due to the uncertainties of real seismic data (e.g. noise, velocity error, anisotropy, etc.). Therefore, the mean or average (total sum divided by total samples), median (the middle number from the order of total samples), and mode (the number that appears the most) methods are introduced for considering the optimum chi angle at each target parameter logs.

For example in **Figure 4.1**, the average or mean angle from all wells is 37 degree (deg), the average or mean angle from similarly 3 wells (A1, A2, & A4) is 45 degree, the median and the mode from all wells are similarly 44 degree. Well A8 has uncommon chi angle because, if this is a reason, it is water-bearing well, so it could be cut out from considerations. The averaging of chi angle from well A1, A2, and A4 is optimal and then the mean, median and mode values are relatively equivalent which make 44 degree being an optimum chi angle for Sw logs.

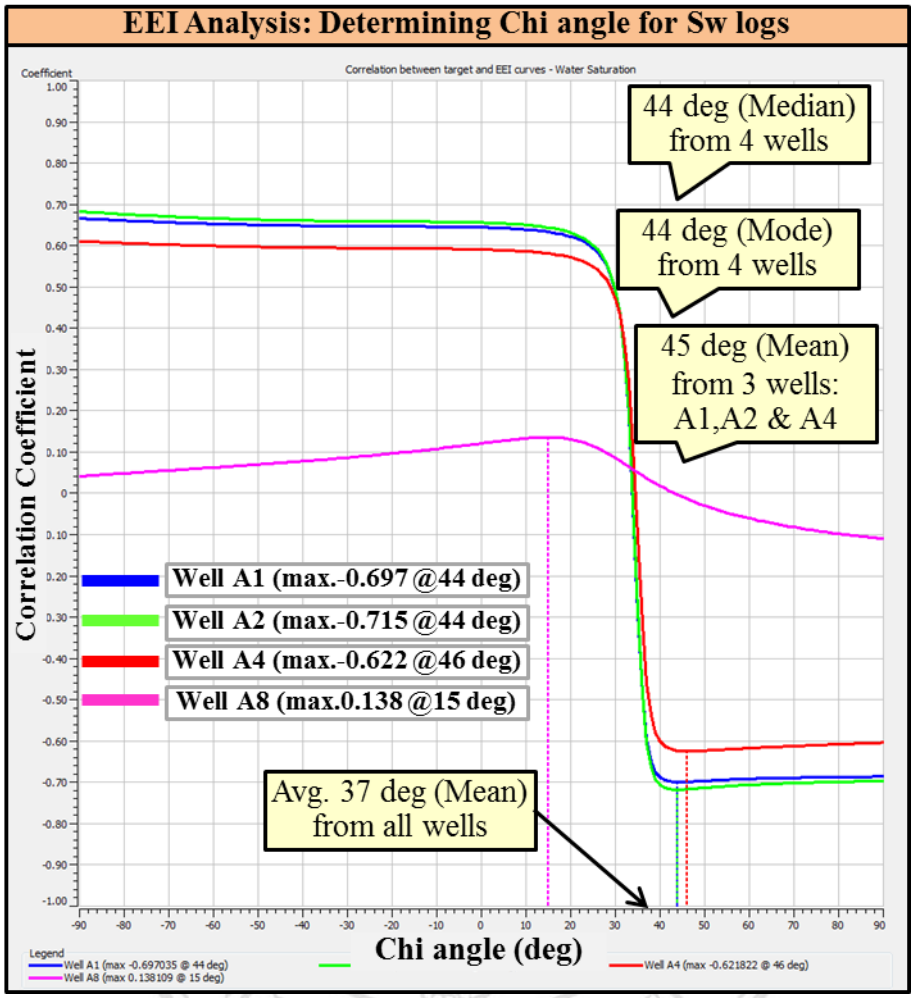

Figure 4.1. The EEI correlation result and the example of mean, median, and mode methods to derive the optimum chi angle for the water saturation (Sw) log.

First of all, the correlations between EEI and target parameter logs which are Sw, Vp/Vs ratio, and Poisson's ratio provide relatively the adjacent chi angles (**Figure 4.2** – **Figure 4.3**). In **Figure 4.2** and **Figure 4.3**, there are the EEI cross-correlations for Sw logs (A), for Vp/Vs ratio logs (B), and for Poisson's ratio (C) which show the mean, median, and mode values of chi angles. The optimum chi angles, highlighted by bold font in yellow rectangular callouts, for Sw, Vp/Vs ratio, and Poisson's ratio logs are 44, 38, and 38 degree having maximum correlation of -0.68, 1, and 0.99 respectively which correspond to the optimum's methods.

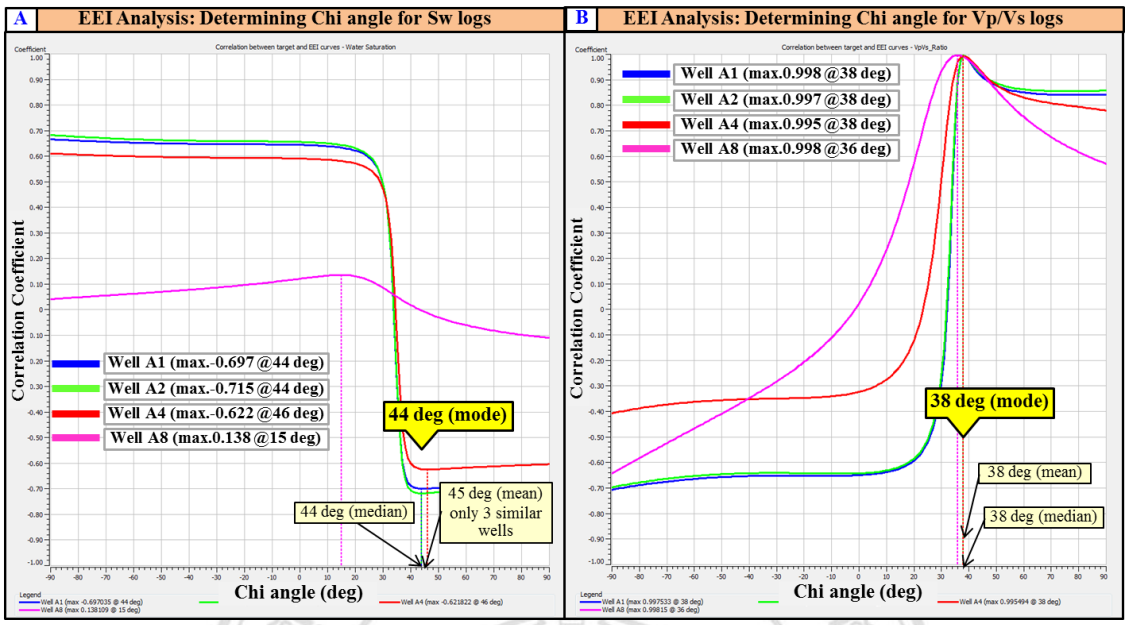

Figure 4.2. The schematic of EEI analysis shows (A) correlation between EEI and Sw logs and (B) EEI and Vp/Vs ratio logs. The optimum chi angles are indicated by yellow rectangular callouts.

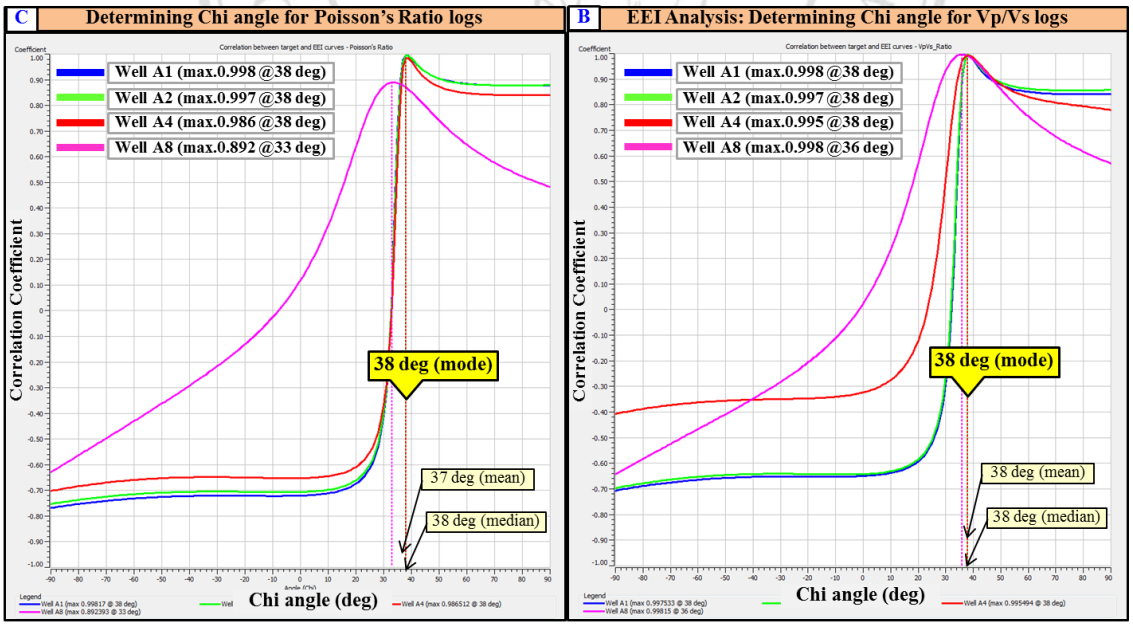

Figure 4.3. The schematic of EEI analysis shows (C) correlation between EEI and Poisson's ratio logs and (B) EEI and Vp/Vs logs. The same optimum chi angle (38 deg) is obtained which indicated by yellow rectangular callouts.

Next, the optimum chi angle determinations for bulk modulus and shear modulus are illustrated in **Figure 4.4** at which the 16 and -58 degree stand for the angle selections. They were picked by using median method for bulk modulus logs and using mean for shear modulus logs. Their maximum coefficients are the same, that is 1.

The optimum chi angles for lambda-rho and mu-rho logs are 25 and -13 degree which represent mode and mean values respectively (**Figure 4.5**). There are the same maximum coefficient of 1.

In Figure **4.6**, the best angles are mostly -56 degree for computed K or $(Vs/Vp)^2$, which these K values were computed simultaneously from the logs, and -82 degree for S-wave impedance (Zs). Their maximum coefficients are similarly 1.

The selected chi angles for volume of clay (VCL) logs and neutron porosity (NPHI) logs are 44 and -67 degree corresponding median and mean methods respectively (**Figure 4.7**). The maximum coefficient of VCL logs is 0.80 as used median samples. The latter's maximum coefficient is -0.85.

To sum up, all chi angles, optimum chi angles, used methods, and item number corresponding to those figures were summarized in **Table 5.** Their maximum correlation coefficients and other were also summarized in **Table 6**.

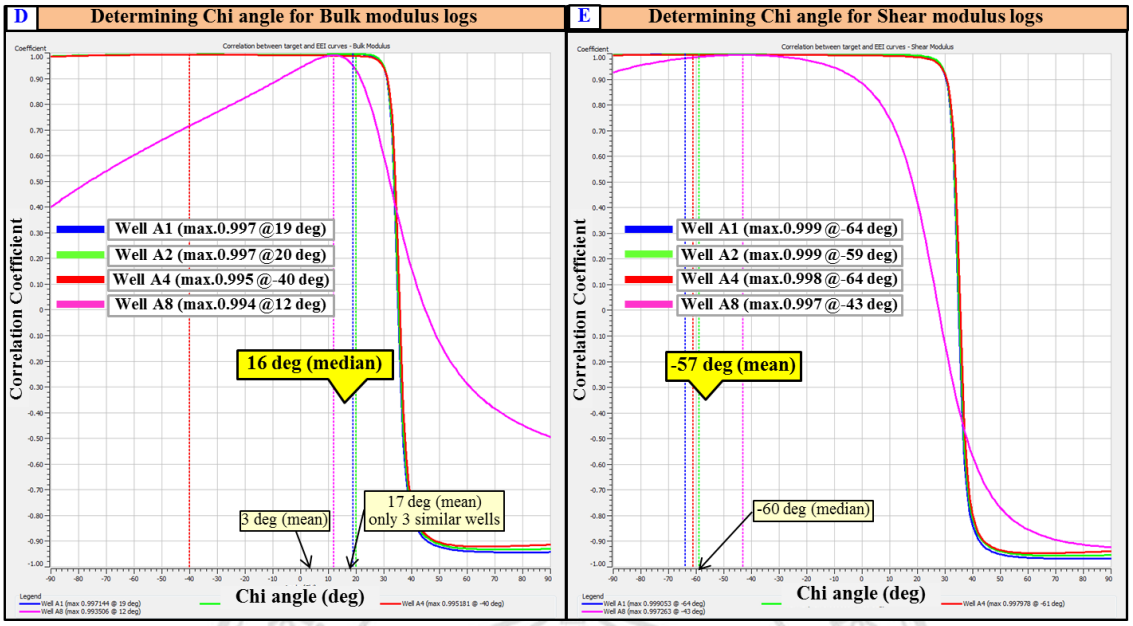

Figure 4.4. The schematic of EEI analysis shows (D) correlation between EEI and Bulk modulus logs and (E) EEI and Shear modulus logs. The optimum chi angles are indicated by yellow rectangular callouts.

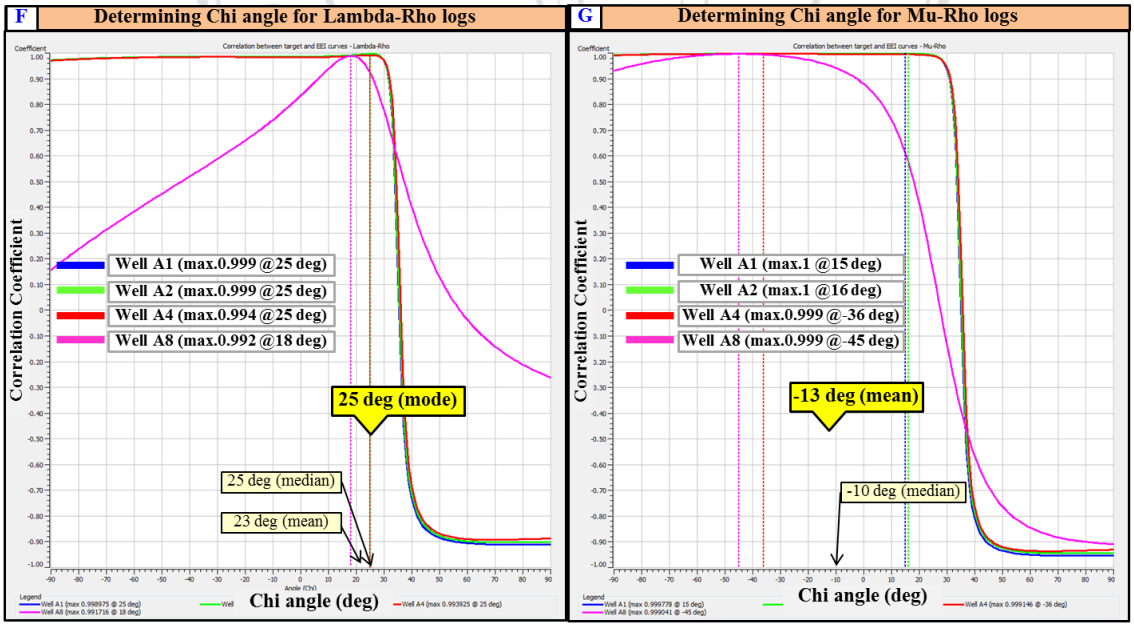

Figure 4.5. The schematic of EEI analysis shows (F) correlation between EEI and Lambda-Rho logs and (G) EEI and Mu-Rho logs. The optimum chi angles are indicated by yellow rectangular callouts.

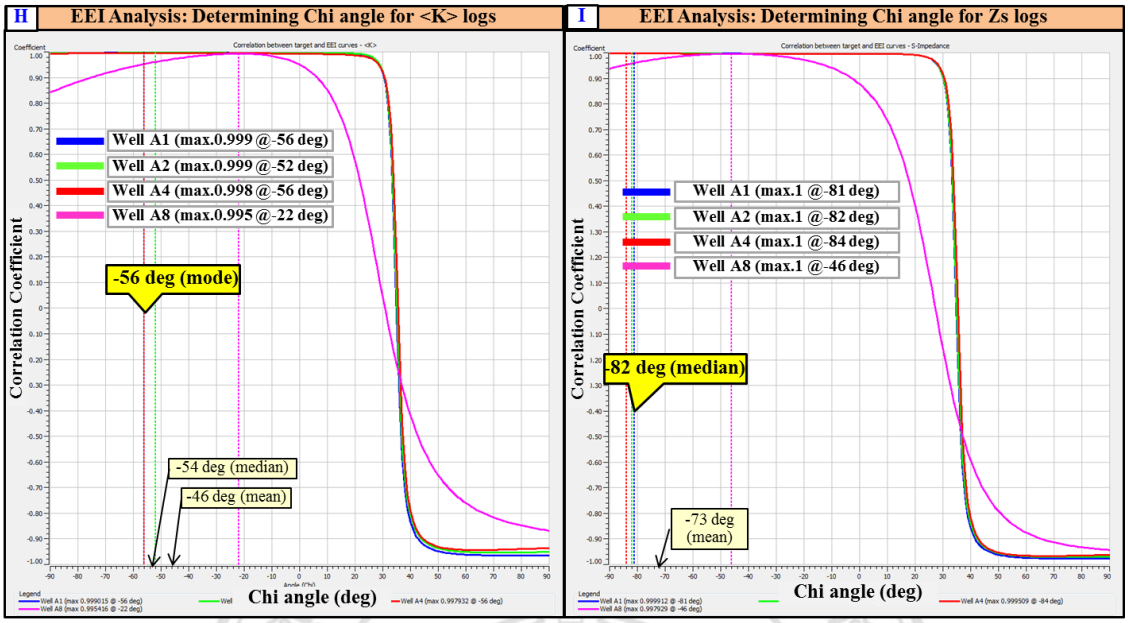

Figure 4.6. The schematic of EEI analysis shows (H) correlation between EEI and $(Vs/Vp)^2$ or <K> logs and (I) EEI and Zs logs. The optimum chi angles are indicated by yellow rectangular callouts.

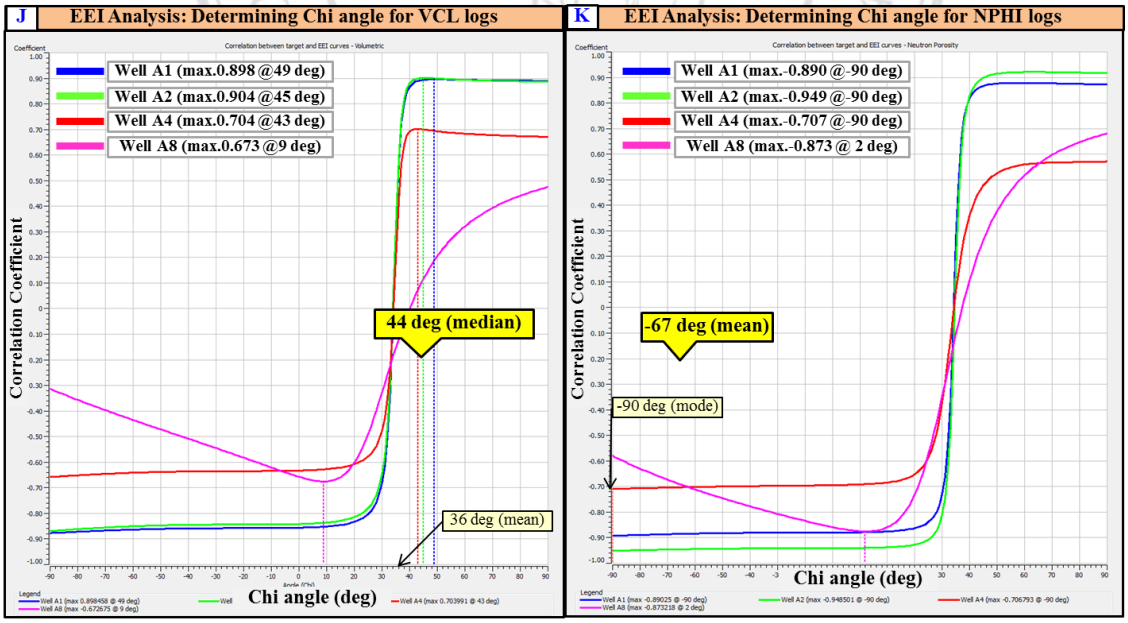

Figure 4.7. The schematic of EEI analysis shows (J) correlation between EEI and VCL logs and (K) EEI and NPHI logs. The optimum chi angles are indicated by yellow rectangular callouts.

Table 4.1. The chi angle determination results showing individual and optimum chi angles with relevant used-methods and item numbers.

Target well logs	Chi angle (deg)					Note	Item No.
	Well A1	Well A2	Well A4	Well A8	Optimum		
Sw	44	44	46	15	44	Mode	A
Vp/Vs ratio	38	38	38	36	38	Mode	B
Poisson's ratio	38	38	38	33	38	Mode	C
Bulk modulus	19	20	-40	12	16	Median	D
Shear modulus	-64	-59	-61	-43	-57	Mean	E
Lambda-Rho	25	25	25	18	25	Mode	F
Mu-Rho	15	16	-36	-45	-13	Mean	G
<K>	-56	-52	-56	-22	-56	Mode	H
S-wave Impedance (Zs)	-81	-82	-84	-46	-82	Median	I
VCL	49	45	43	9	44	Median	J
Neutron Porosity (NPHI)	-90	-90	-90	2	-67	Mean	K

Table 4.2. The results of individual and optimum maximum coefficients with relevant used-methods and item numbers.

Target well logs	Maximum Coefficient					Note	Item No.
	Well A1	Well A2	Well A4	Well A8	Optimum		
Sw	-0.697	-0.715	-0.622	0.138	-0.68	Mode	A
Vp/Vs ratio	0.998	0.997	0.991	0.998	1.00	Mode	B
Poisson's ratio	0.998	0.997	0.987	0.892	0.99	Mode	C
Bulk modulus	0.997	0.998	0.995	0.994	1.00	Median	D
Shear modulus	0.999	0.999	0.998	0.997	1.00	Mean	E
Lambda-Rho	0.999	0.999	0.994	0.992	1.00	Mode	F
Mu-Rho	1	1	0.999	0.999	1.00	Mean	G
<K>	0.999	0.999	0.998	0.995	1.00	Mode	H
S-wave Impedance (Zs)	1	1	1	0.998	1.00	Median	I
VCL	0.898	0.904	0.704	-0.673	0.80	Median	J
Neutron Porosity (NPHI)	-0.890	-0.949	-0.707	-0.873	-0.85	Mean	K

To validate all optimum chi angles, they were compared to researches of Whitcombe et al. (2002) and Shahri A. (2013) showing in **Table 7**.

From **Table 7**, it can be concluded that all results in this study are reliable at which most optimum chi angles are adjacently to other results including the water saturation, Vp/Vs ratio, Poisson's ratio, bulk modulus, shear modulus, lambda-rho, and porosity logs.

Table 4.3. The comparison among optimum chi angle results, and other researches (Whitcombe et al, 2002, and Shahri A, 2013).

Target well logs	Maximum Coefficient	Chi angle (deg)		
		Optimum	Whitcombe et al.(2002)	Shahri A. (2013)
Sw	-0.68	44	-	43
Vp/Vs ratio	1.00	38	45	39
Poisson's ratio	0.99	38	-	34
Bulk modulus	1.00	16	12	18
Shear modulus	1.00	-57	-58	-53
Lambda-Rho	1.00	25	20	24
Mu-Rho	1.00	-13	-	-42
<K>	1.00	-56	-	-
S-wave Impedance (Zs)	1.00	-82	-45	-36
VCL	0.80	44	-	13
Neutron Porosity (NPHI)	-0.85	-67	-	-

4.2 EEI log and reflectivity

4.2.1 EEI log

After getting the optimum chi angles related to selected logs, the calculation of EEI logs will be conducted using EEI equation or Equation 2.8 (Whitcombe et al., 2002). The required parameters for calculating targeted EEI logs are well logs such as P-wave, S-wave, and density (Vp, Vs, & ρ), optimum chi (χ) angle, and computed K (Vs^2/Vp^2), which was calculated simultaneously from the well. The targeted EEI logs consist of Vp/Vs, Poisson's ratio (PR), bulk modulus, shear modulus, lambda-rho (λρ), mu-rho (μρ), S-wave impedance (Zs), volume of clay (VCL), and neutron porosity (NPHI). Their units are in impedance (m/s)*(g/cm3).

Accordingly, the calculated EEI logs from all wells are plotted in order to compare with the original target parameter logs for quality control (**Figure 4.8 – Figure 4.12**) at which the zone of hydrocarbon, from Base Fiqa to Natih E, were displayed. In those Figures, the vertical scales are two-way time (TWT) in ms on the left, true vertical depth (TVD) from surface in m on the right, and the EEI scaling factor in impedance was adjusted individually at well A2 as reference, then all adjusted-impedance scales would be applied at other wells.

In **Figures 4.8, 4.9**, and **4.10**, there are the oil-bearing reservoirs highlighted by green rectangles on the left of gamma ray log and the oil-down-to (ODT) level at each well depicted by green-dotted line. These oil-bearing carbonate reservoirs are characterized by low Vp/Vs (1.84-1.86), low Poisson's ratio (0.29-0.30), low-moderate bulk modulus (23-34 GPa), low shear modulus (11 – 17 GPa), low lambda-rho (38-58 $GPa*g/cm^3$), and low mu-rho (26-42 $GPa*g/cm^3$).

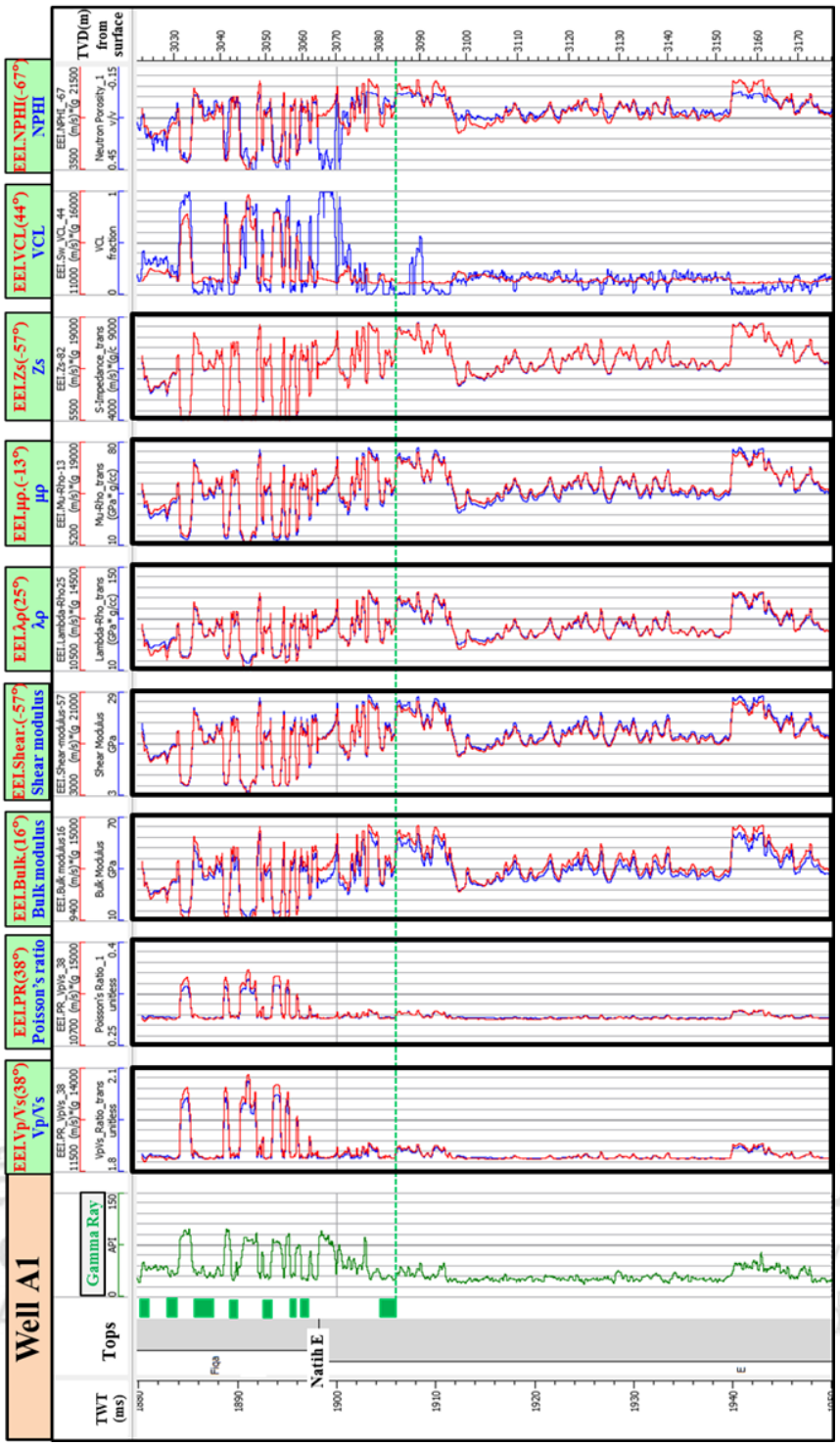

Figure 4.8. The schematic of calculated EEI logs (red curves) overlaid on original target parameter logs (blue curves) for well A1 which included GR, Vp/Vs, Poisson's ratio (PR), bulk modulus, shear modulus, lambda-rho (λρ), mu-rho (μρ), S-wave impedance (Zs), volume of clay (VCL), and neutron porosity (NPHI). Two logs tracked very well together highlighting by black rectangles.

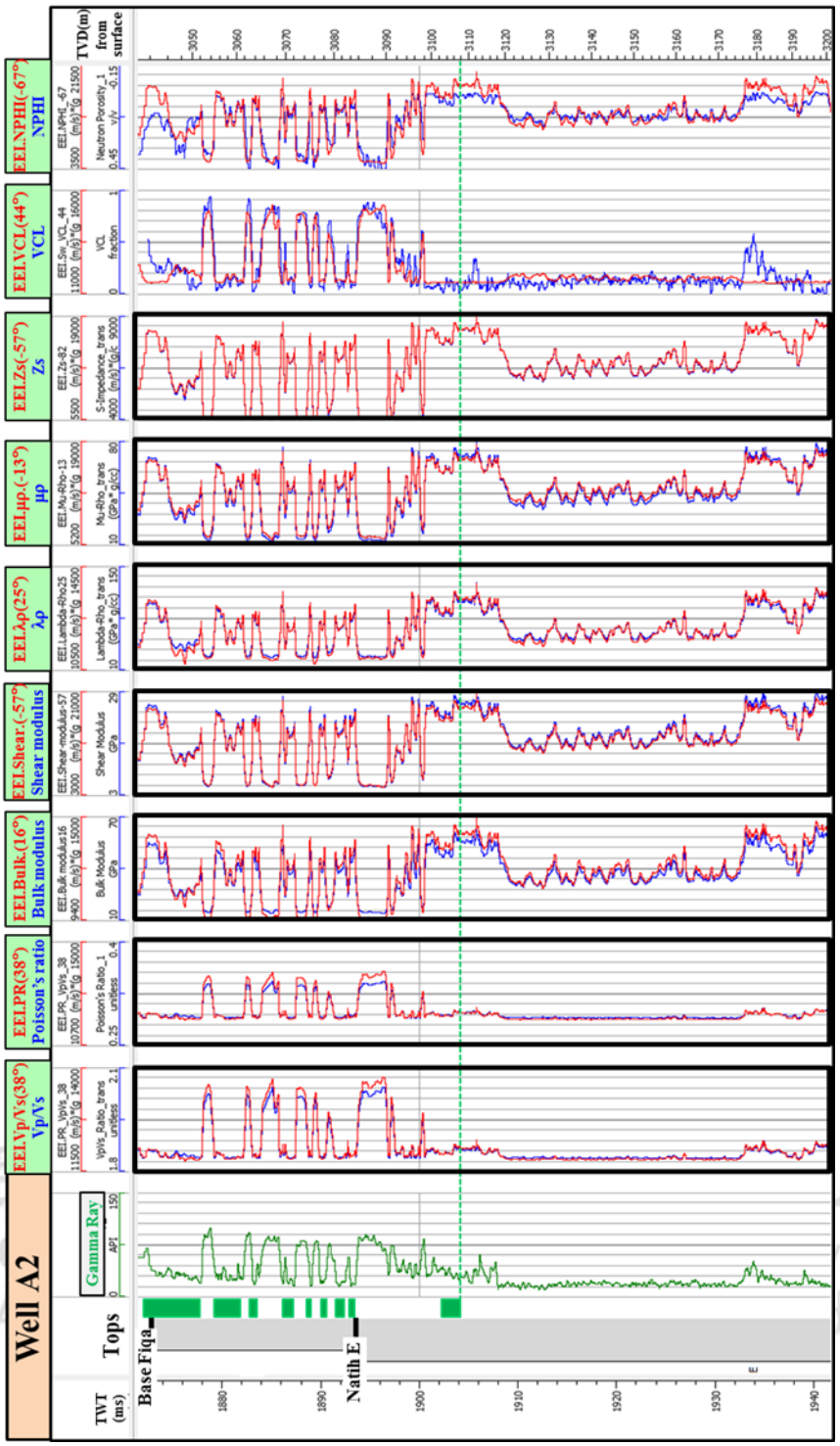

Figure 4.9. The schematic of calculated EEI logs (red curves) overlaid on original target parameter logs (blue curves) for well A2 which included GR, Vp/Vs, Poisson's ratio (PR), bulk modulus, shear modulus, lambda-rho (λρ), mu-rho (μρ), S-wave impedance (Zs), volume of clay (VCL), and neutron porosity (NPHI). Two logs tracked very well together highlighting by black rectangles.

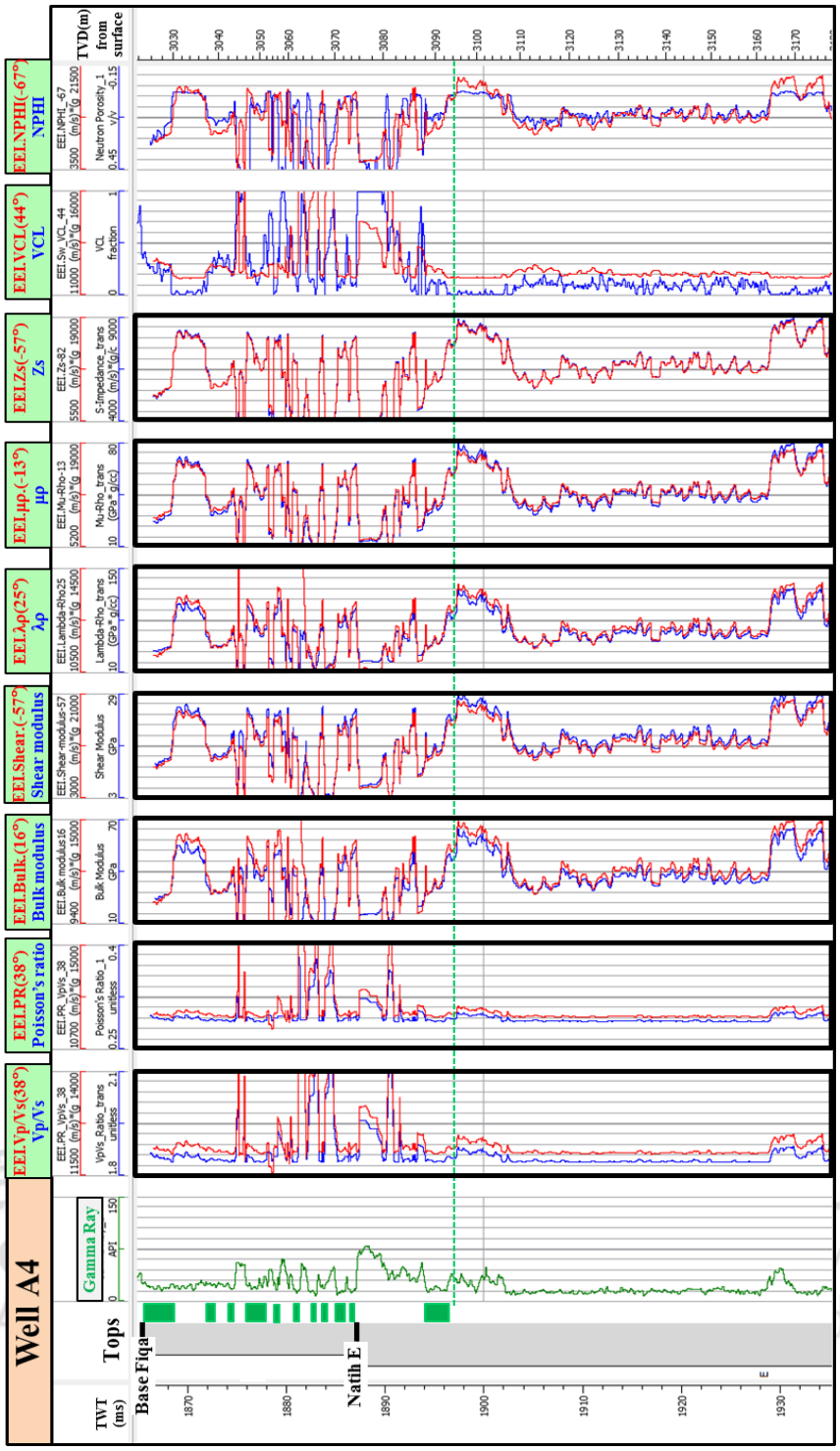

Figure 4.10. The schematic of calculated EEI logs (red curves) overlaid on original target parameter logs (blue curves) for well A4 which included GR, Vp/Vs, Poisson's ratio (PR), bulk modulus, shear modulus, lambda-rho (λρ), mu-rho (μρ), S-wave impedance (Zs), volume of clay (VCL), and neutron porosity (NPHI). Two logs tracked very well together highlighting by black rectangles.

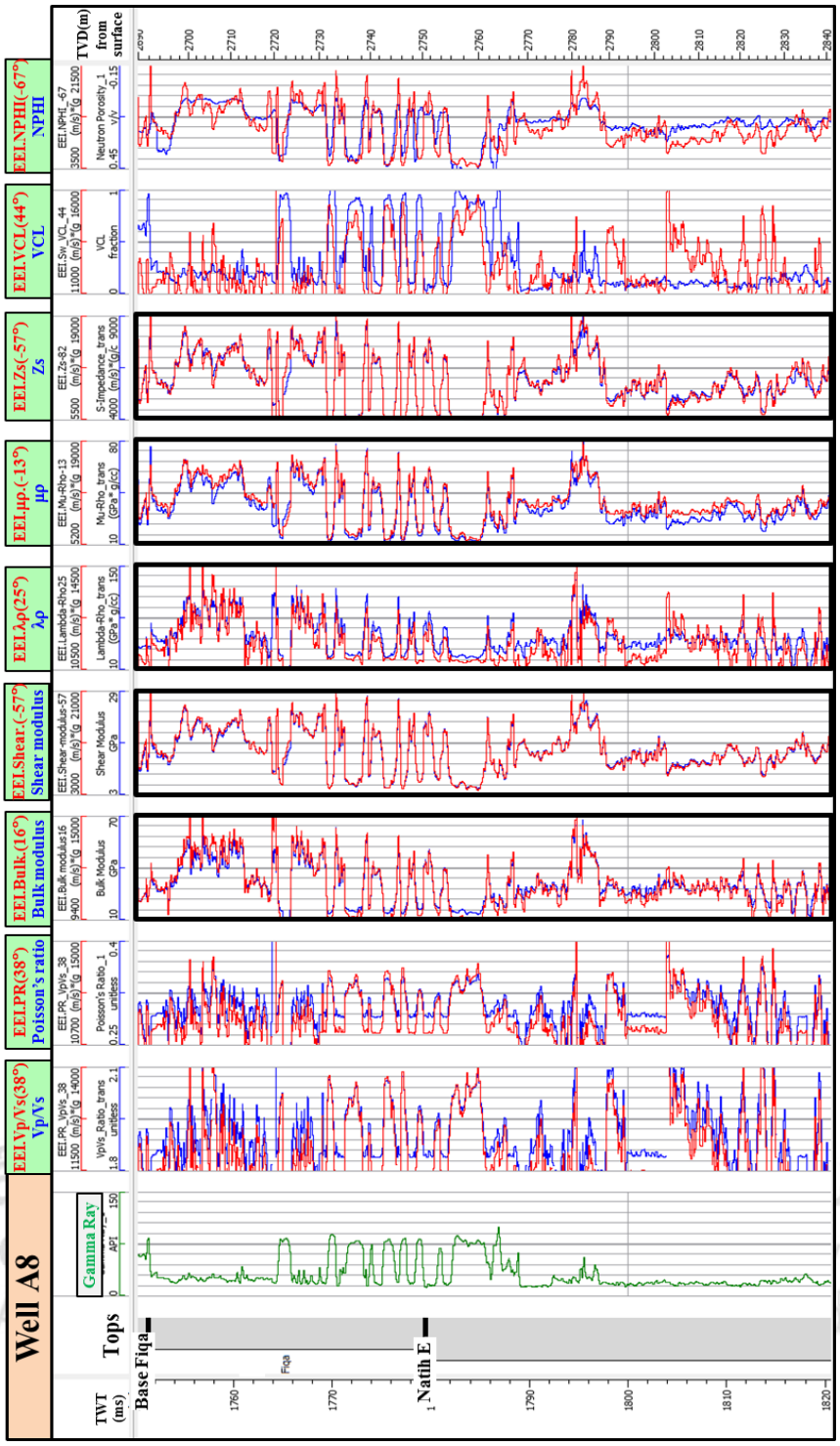

Figure 4.11. The schematic of calculated EEI logs (red curves) overlaid on original target parameter logs (blue curves) for well A8 with same scale. Two logs tracked very well together highlighting by black rectangles.

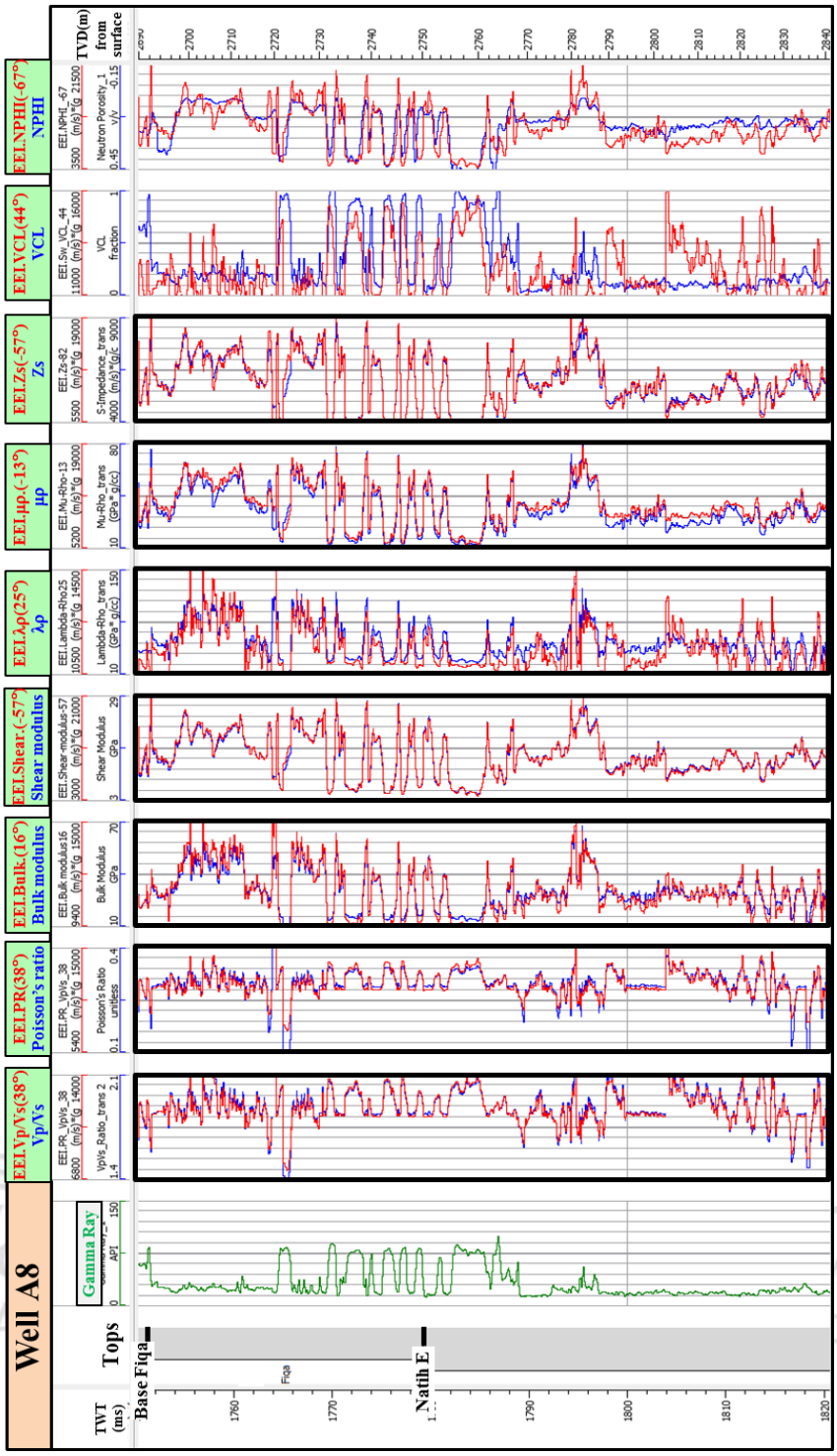

Figure 4.12. The schematic of calculated EEI logs (red curves) overlaid on original target parameter logs (blue curves) for well A8 with different scale of EEI logs. Two logs tracked very well together highlighting by black rectangles.

With reference to those schematics (**Figure 4.8 – Figure 4.12**), it is clearly that the most of EEI logs calculated at selected chi angle tracked very well with the original target logs especially the EEI Vp/Vs (38 degree or 38°), EEI Poisson's ratio (38°), the EEI bulk (16°) and EEI shear (-57°) moduli, the EEI $\lambda\rho$ (25°), EEI $\mu\rho$ (-13°), and EEI Zs (-82°) which were highlighted by black rectangles.

The general exceptions occur in the EEI VCL versus VCL and the EEI NPHI versus NPHI panels at all schematics (**Figure 4.8 – Figure 4.12**). The main reason for these exceptions is that there are the lowest cross-correlations (0.80 and -0.85 for VCL and NPHI logs respectively). The non-agreements in the EEI Vp/Vs (38°) versus Vp/Vs and the EEI PR (38°) versus PR at well A8 (**Figure 4.11**) expose apparently and the possible reason of them is that the use of mode value in chi angle determination. To overcome these non-agreements at well A8, the other scaling factors attempted in **Figure 4.12**, then the curves of EEI Vp/Vs (38°) versuse Vp/Vs and the curves of EEI PR (38°) versus PR now tracked very well.

A very good match between the calculated EEI and target curves indicates that not only those selected (optimum) chi angles are significantly reliable for target parameter logs, but the derived-EEI parameter logs can be used also for quantitative interpretation.

4.2.2 EEI reflectivity

Next step is to compute the targeted EEI reflectivity (REEI) volumes with Equation 2.9 by using intercept (A) and gradient (B) AVO attributes volumes, which had been done in section 3.3, and the optimum chi angle of desired target log.

In this study, the four REEI volumes have been computed by applying the optimum chi angles of 16°, 25°, 38°, and -13° as shown in **Table 8** for each desired target.

Table 4.4. The summary of the computed EEI reflectivity (REEI) volumes.

REEI volume no.	Chi (χ) angle used (degree)	Desired target parameter log
1	16	Bulk modulus
2	25	Lambda-Rho
3	38	Poisson's ratio
4	-13	Mu-Rho

After the computed REEI volumes obtained, their sections at inline 2618 are illustrated in **Figure 4.13** and **Figure 4.14** including the volumes of REEI bulk modulus (A), REEI Poisson's ratio (B), REEI lambda-rho (C), and REEI mu-rho (D). The vertical scale is two-way time in ms and color key ranges between -1.00 to 1.00 representing P-wave gradient as displayed in those figures.

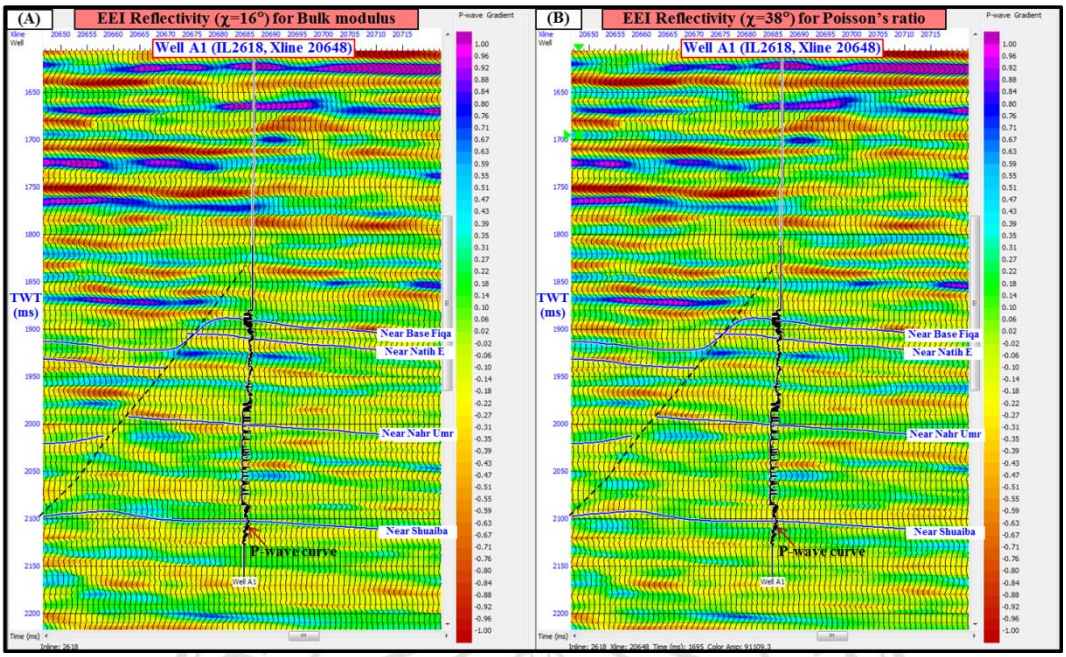

Figure 4.13. The computed EEI reflectivity (REEI) sections at inline 2618 overlaid by well A1's P-wave curve, which includes (A) the REEI bulk modulus, and (B) the REEI Poisson's ratio.

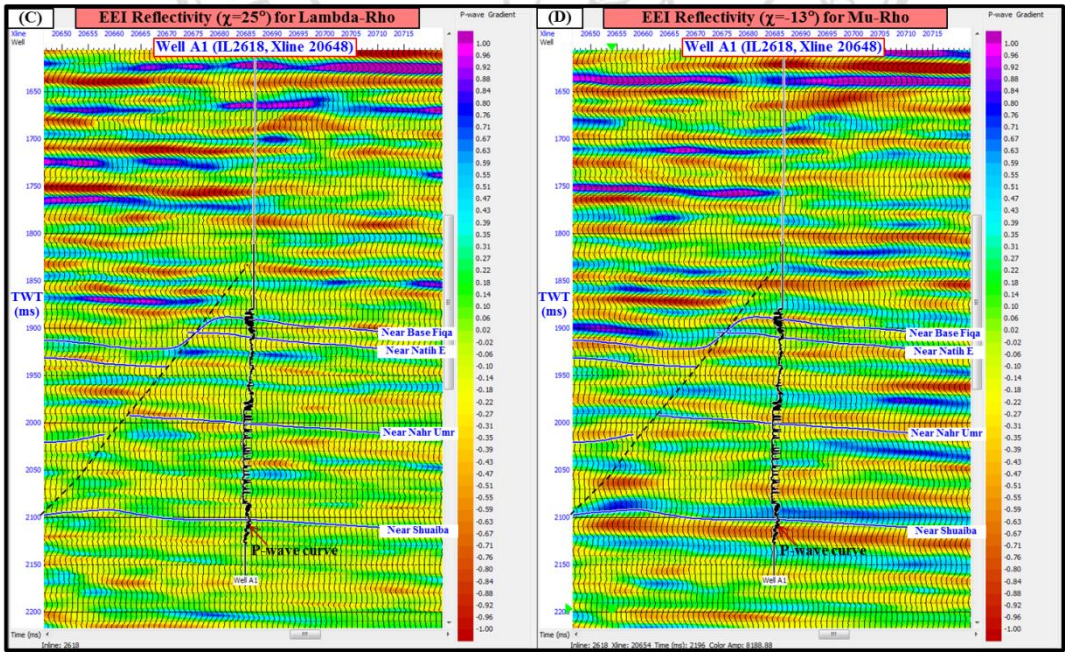

Figure 4.14. The computed EEI reflectivity (REEI) sections at inline 2618 overlaid by well A1's P-wave curve, which includes (C) the REEI lambda-rho, and (D) the REEI mu-rho.

4.3 EEI inversion

4.3.1 Post-stack inversion and analysis

After the computation of EEI reflectivity volumes, the following step is to perform the post-stack seismic inversion and analysis. In this step, the strata model of elastic impedance inversion was typically built by using the well logs of density, elastic impedance, P-wave, and S-wave. Then the wavelet extractions from the desired reflectivity volumes were performed.

As mentioned in section 3.2.1 (Chapter 3), there are 2 basic methods of wavelet extraction in the Hampson-Russell software including first method integrates the wells to extract from desired seismic volume, which is namely "wavelet use tied-wells", and second method extracts from seismic volume alone, that is namely "statistical wavelet".

In this post-stack inversion analysis, at first step, three extracted wavelets were generated which consist the wavelet use 4 tied-wells from REEI of chi 16° volume, or REEI.16 volume (A), the wavelet use 3 tied-wells from REEI.16 volume (B), and the statistical wavelet extracted alone from REEI.16 volume (C). In the next step, the model-based post-stack inversion has been performed by using those wavelets in order to compare and contrast the synthetic correlation, P-wave impedance (Zp) error, and inverted summary, which then was illustrated in **Figure 4.15**.

In **Figure 4.15,** the profile-plots compare three types of applied wavelet in the post-stack inversion analysis which consists of (A) wavelet use 4 tied-wells from REEI.16 volume (A), wavelet use 3 tied-wells from REEI.16 volume (B), and -57° phase-statistical wavelet from REEI.16 volume (C). They are similar values of synthetic correlation (0.997), synthetic error (0.078 to 0.083), and Zp error (205 to 208) in **Figure 4.15**. To select the satisfied wavelet to perform inversion, the comparison was made in **Figure 4.16** that post-stack inversion analysis at well A1 used several wavelets were illustrated. As **Figure 4.16** exposed the statistical wavelet (-57°) from REEI.16 volume shows clearly small Zp errors and good fit between predicted (red) and real (blue) curves. Therefore, this wavelet is selected to carry on the post-stack inversion.

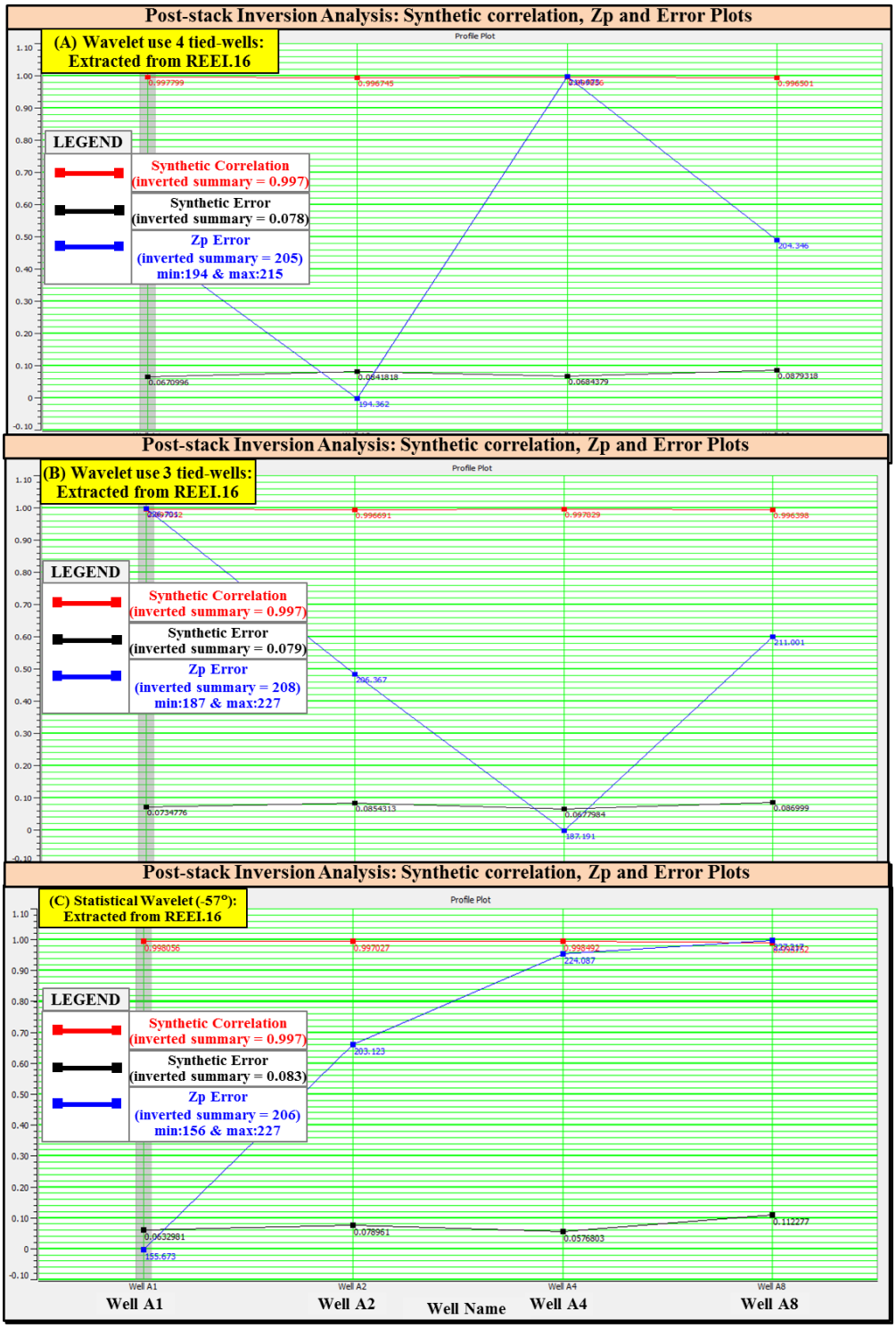

Figure 4.15. The profile-plots comparing three types of applied wavelet in the post-stack inversion analysis which consists of (A) wavelet use tied-wells from original seismic volume, (B) wavelet use tied-wells from REEI.16 volume, and (C) statistical wavelet with -57° from REEI.16 volume.

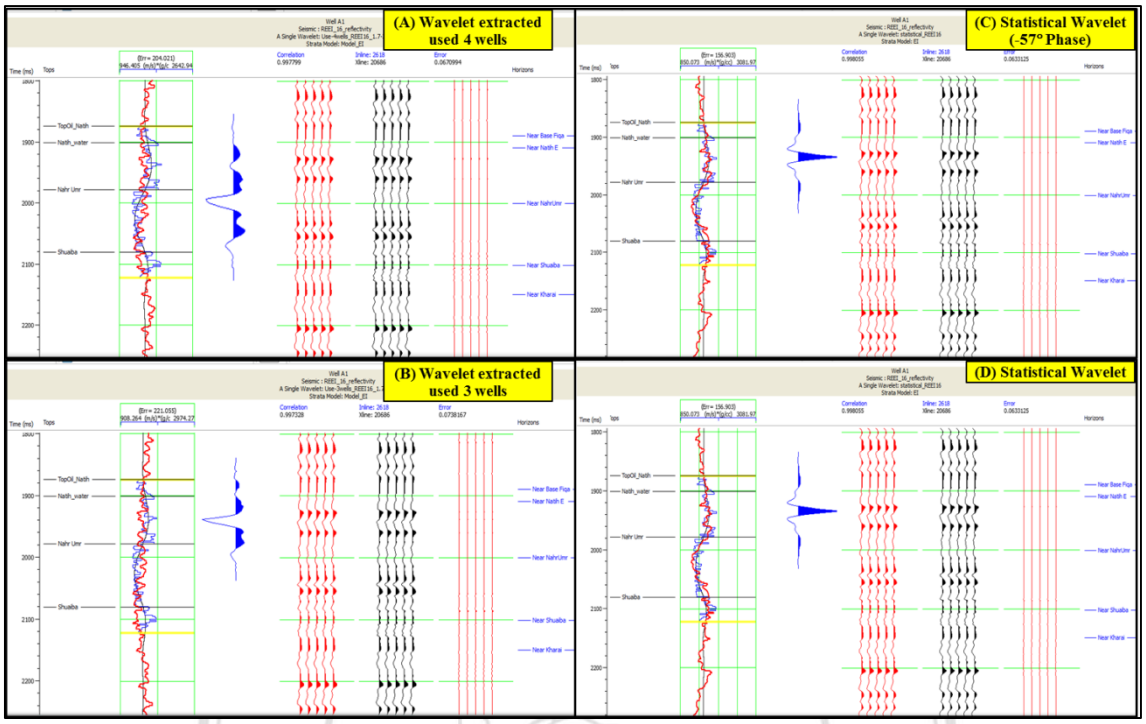

Figure 4.16. The comparison among different wavelets used in the post-stack inversion analysis.

As **Figure 4.16** illustrated the same initial model can generate different results which is commonly known as the non-uniqueness of inversion. After the selection of extracted wavelet for REEI.16 volume, the model-based post-stack inversion was run using 100 iterations. The resultant analysis plots were displayed in **Figures 4.17**, **4.18**, and **4.19**, which are for well A1, A2, and A4 respectively.

In **Figure 4.17**, the post-stack inversion analysis plot at well A1 was illustrated in which there are, from left to right, the tracks of tops, P-wave impedance (Zp) comparison, used-wavelet, synthetic, seismic trace, and error. The synthetic correlation is 0.999 with 0.046 of error and RMS Zp error is totally 165.276 m/s*g/cm3. The error calculated from the difference between original seismic trace, in this case is REEI.16, and synthetic trace.

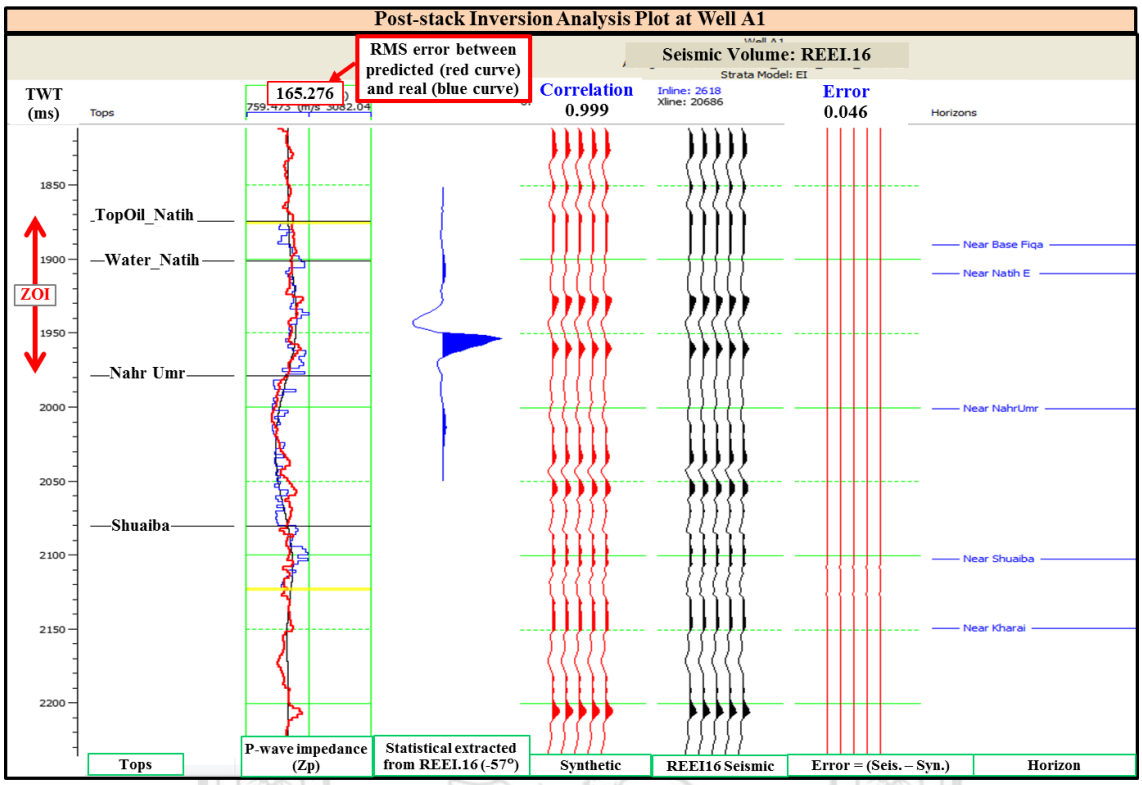

Figure 4.17. The post-stack inversion analysis plot at well A1 includes (from left to right) the tracks of tops, Zp comparison, used-wavelet, synthetic, seismic trace, and error. The synthetic correlation is 0.999 with 0.046 of error and RMS Zp error is 165.276 m/s*g/cm3.

In **Figure 4.18**, the post-stack inversion analysis plot at well A2 was illustrated in which there are, from left to right, the tracks of tops, P-wave impedance (Zp) comparison, used-wavelet, synthetic, seismic trace, and error. The synthetic correlation is 0.998 with 0.063 of error and RMS Zp error is totally 210.014 m/s*g/cm3. The error calculated from the difference between original seismic trace, in this case is REEI.16, and synthetic trace.

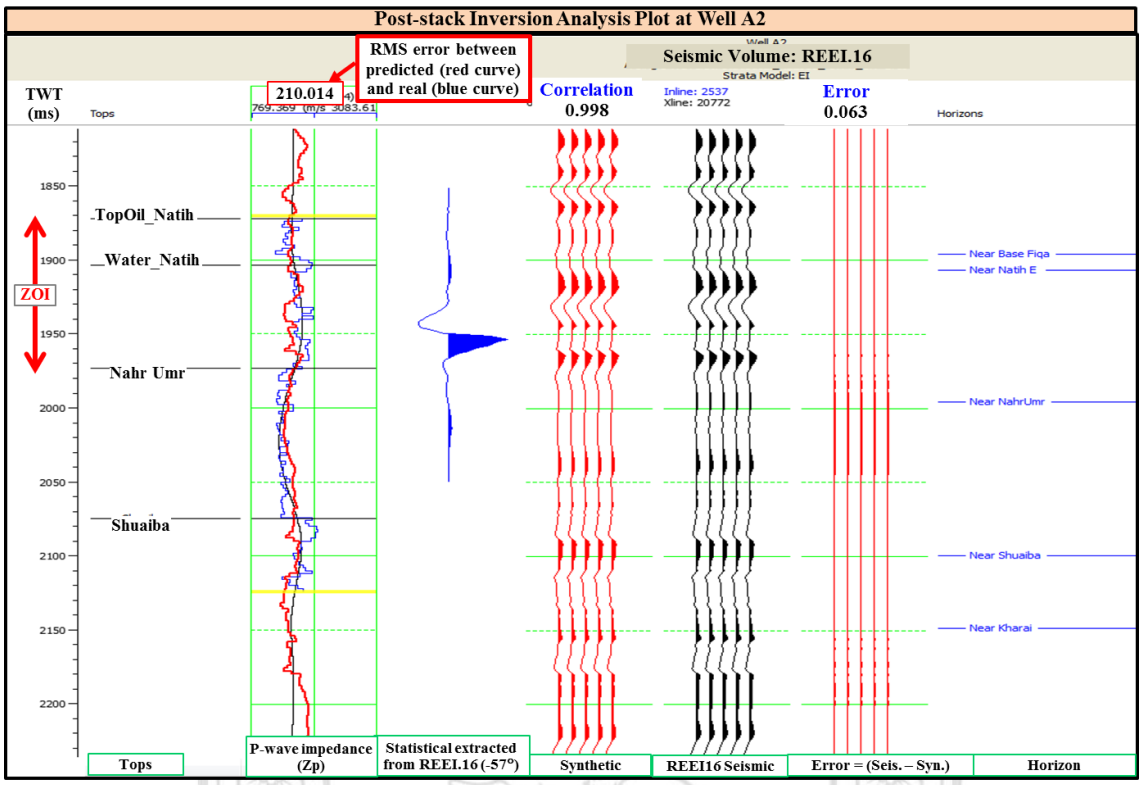

Figure 4.18. The post-stack inversion analysis plot at well A2 includes (from left to right) the tracks of tops, Zp comparison, used-wavelet, synthetic, seismic trace, and error. The synthetic correlation is 0.998 with 0.063 of error and RMS Zp error is 210.014 m/s*g/cm^3.

In **Figure 4.19**, the post-stack inversion analysis plot at well A4 was illustrated in which there are, from left to right, the tracks of tops, Zp comparison, used-wavelet, synthetic, seismic trace, and error. The synthetic correlation is 0.999 with 0.05 of error and RMS Zp error is totally 246.309 m/s*g/cm3.

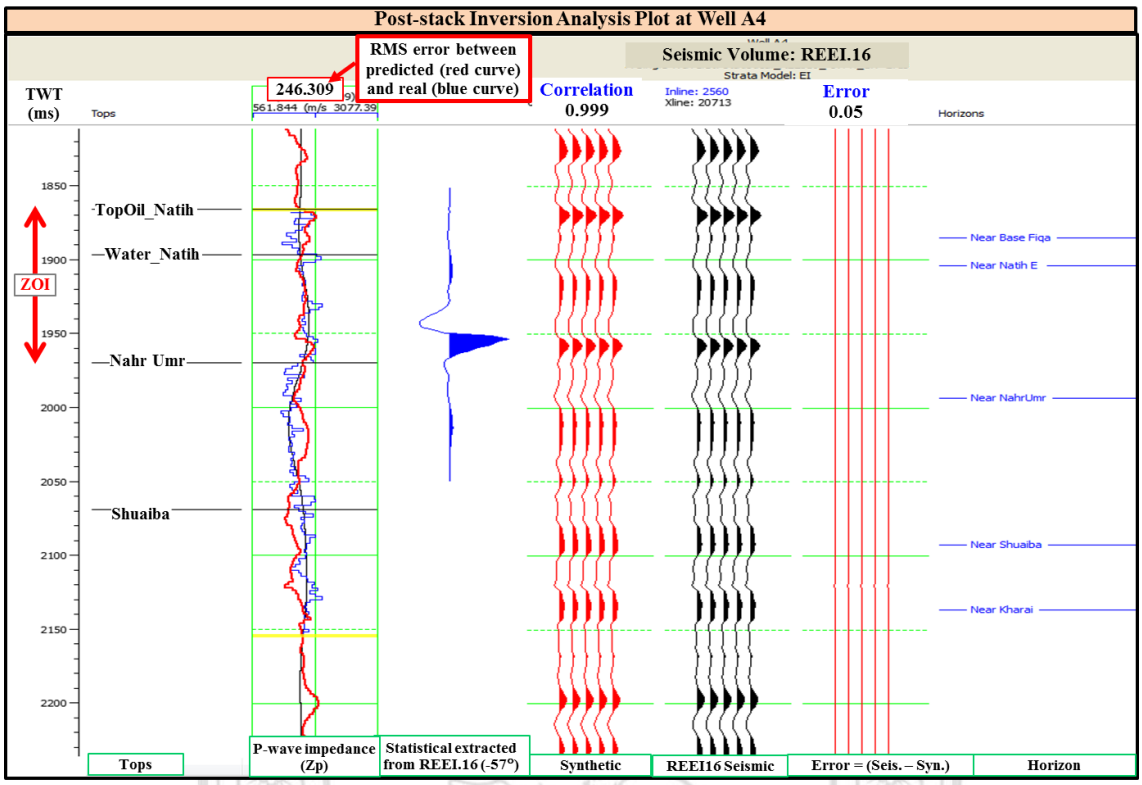

Figure 4.19. The post-stack inversion analysis plot at well A4 includes (from left to right) the tracks of tops, Zp comparison, used-wavelet, synthetic, seismic trace, and error. The synthetic correlation is 0.999 with 0.05 of error and RMS Zp error is 246.309 m/s*g/cm^3.

The following cross-plot of inverted Zp log versus original Zp log was performed and illustrated in **Figure 4.20**, in which the x axis is original Zp log, the y axis is inverted Zp log, and the unit is in m/s*g/cm^3. The linear regression and its error were analyzed, that error is approximately 109 m/s*g/cm^3.

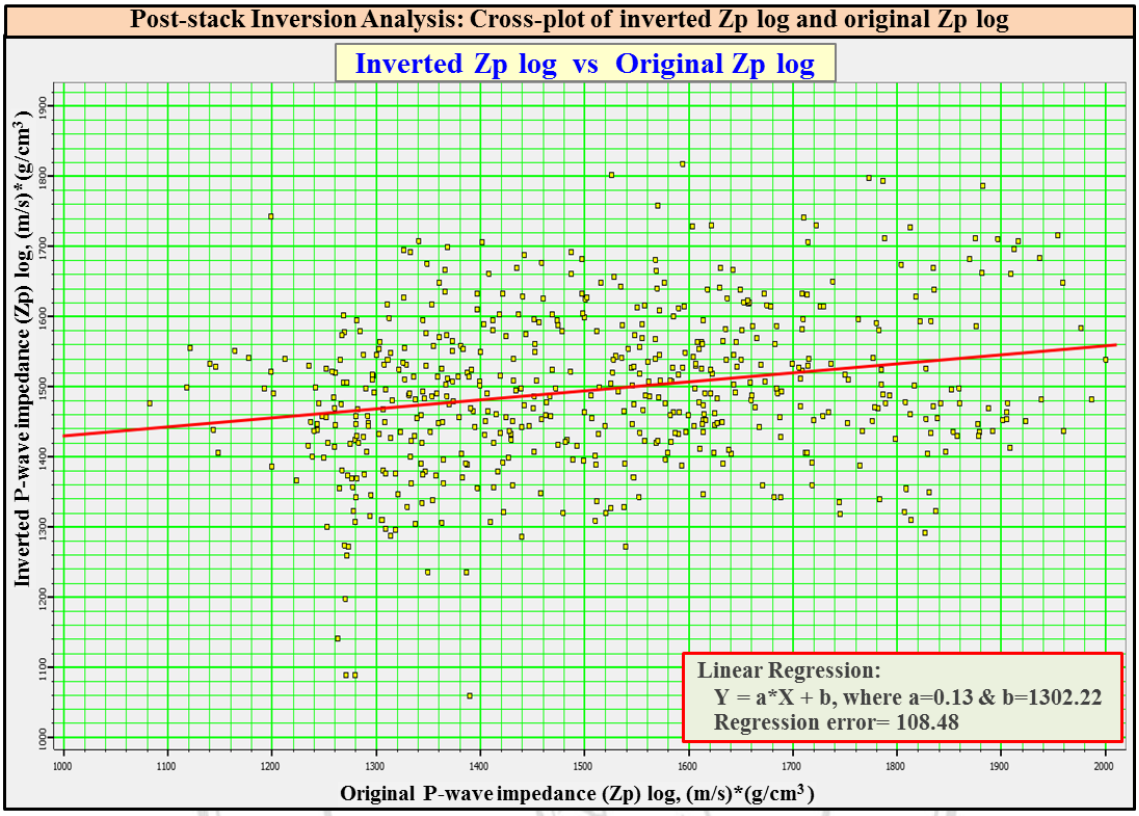

Figure 4.20. The cross-plot of inverted Zp log versus original Zp log calculated from all wells, at which the linear regression and its error were depicted.

As method of model-based post-stack inversion allows us to check until the error is small enough, as mentioned in Chapter 2, these results are satisfactorily with the inverted synthetic correlation of 0.997 and the inverted synthetic error of 0.083, thus the inversion would be run to obtain the impedance of this EEI reflectivity volume.

The same process has been re-done for three remaining REEI volumes, which are REEI.25, REEI.38, and REEI.-13 volumes, including the wavelet extraction, post-stack inversion analysis, and inversion.

4.3.2 EEI inversion

After EEI inversion was performed, the inverted results of EEI reflectivity (REEI) volume at desired chi angle obtained. To yield the compatible scale of inverted EEI volumes at each target parameter, the scaling factors are required to be the multiplier constant (**Figure 4.21**). In **Figure 4.21**, the values of Vp/Vs and EEI.Vp/Vs logs were displayed, highlighted by red circle, at compatible scale, and then the target Vp/Vs would be divided by EEI value to get the constant. This is the multiplier constant (0.000156) that will be applied to the desired inverted-EEI volume for having the similar scale to the target parameter log, in this example which is the inverted-EEI Vp/Vs volume.

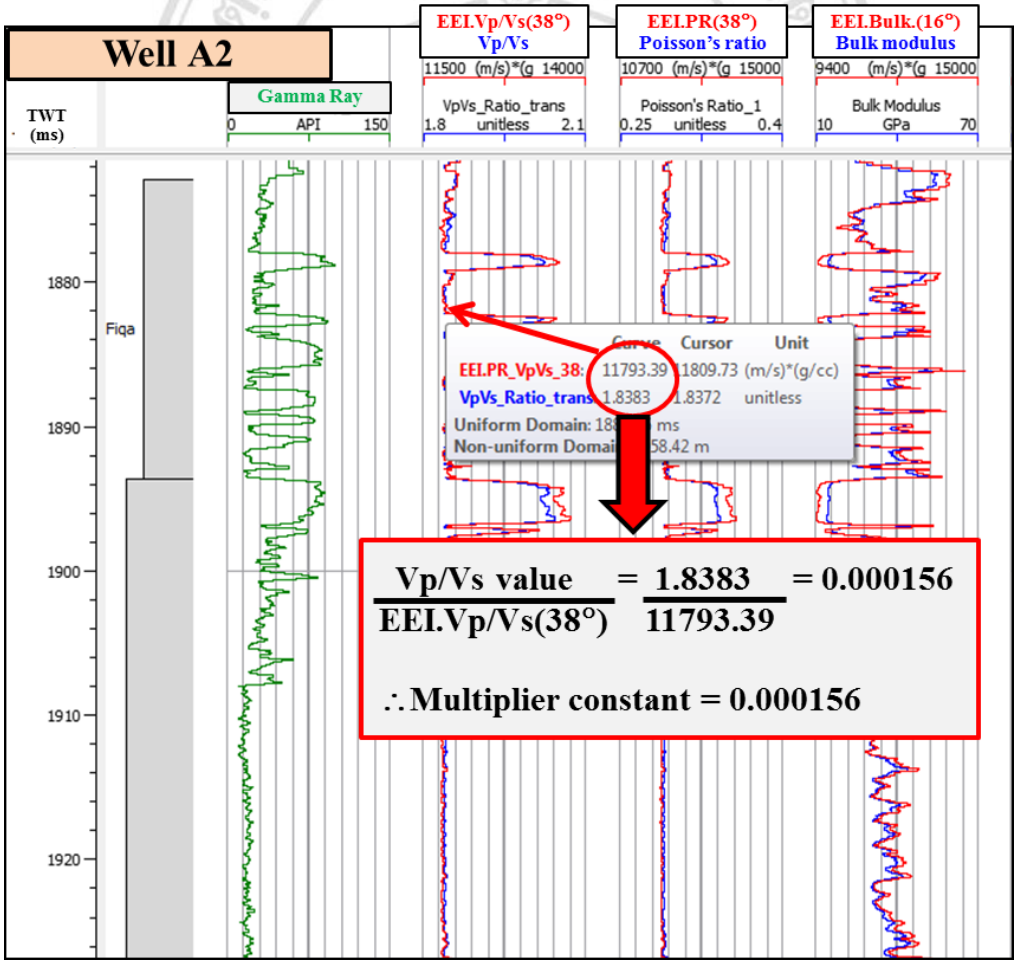

Figure 4.21. The method of determining scaling factor to apply on the desired inverted-EEI volumes, this example is for equivalent Vp/Vs.

4.3.2.1 EEI bulk modulus results

From **Figure 4.22** to **Figure 4.27** show the section views of the inverted-EEI bulk modulus volume (χ=16°) overlaid by the equivalent log for the hydrocarbon wells (well A1, well A2, & well A4) at which the good fit can be seen. From these figures they can be concluded that the results are well defined in aspect of fluid except at well A2.

In the aspect of fluid, the oil-bearing reservoirs, that situated at the top of water-bearing reservoirs at all wells, can be relatively differentiated from water zones, depending on the range of equivalent-EEI (scaled to bulk modulus log) between 23 to 35 GPa*g/cm^3. The expand views of each well, in which the section views of the inverted-EEI bulk modulus volume (χ=16°) overlaid by the equivalent log at well A1, well A2, and well A4 were displayed in **Figure 4.23, Figure 4.25, and Figure 4.27** respectively.

In the aspect of lithology, the limestone sections of Natih and Shuaiba formations can be easily recognized that have the equivalent-EI scales of more than 26 GPa*g/cm^3 (**Figure 4.22, Figure 4.24, & Figure 4.26**). The main thick-shales interbedded with thin limestones of Nahr Umr formation can also be distinguished extraordinarily (**Figure 4.22, Figure 4.24, & Figure 4.26**) due to the uncommon EI values (less than 27 GPa*g/cm^3).

Figure 4.28 shows the arbitrary view across well A1, well A4, and well A2 that this inverted-EEI bulk modulus volume provides the different characteristics for identifying the fluid types in the carbonate reservoirs of the Natih formation.

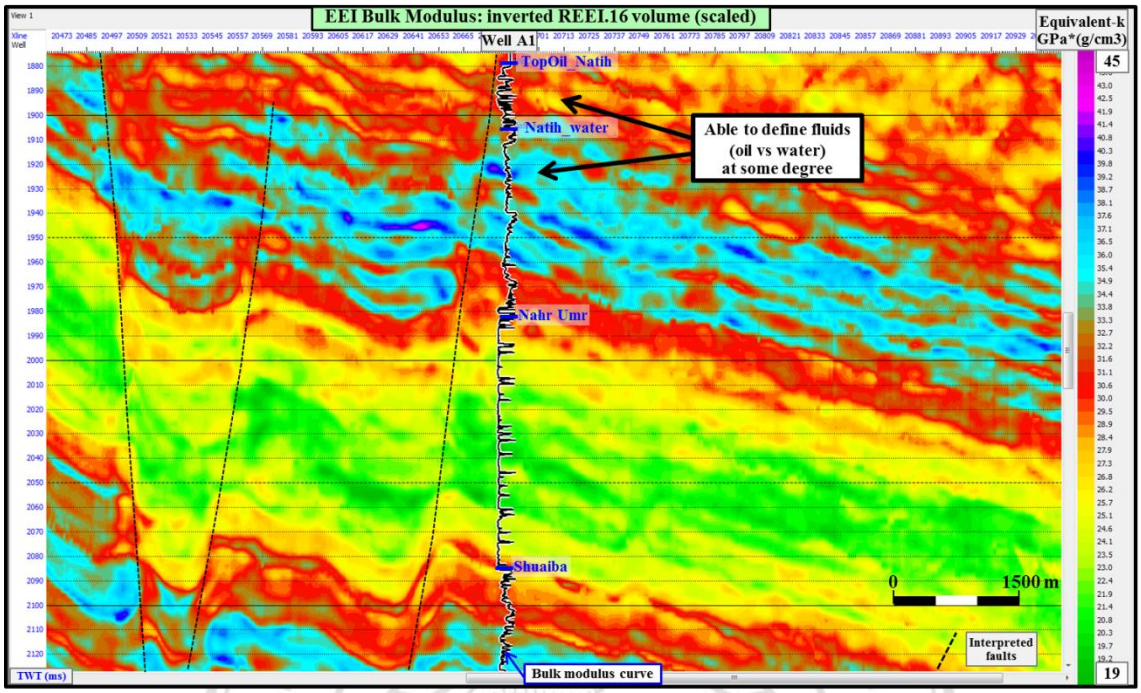

Figure 4.22. The section view of inverted-EEI bulk modulus volume (χ=16°) shows at well A1 with bulk modulus curve. The fluid (oil versus water) and lithology (limestones versus thick-shales interbedded thin-limestone) are well defined.

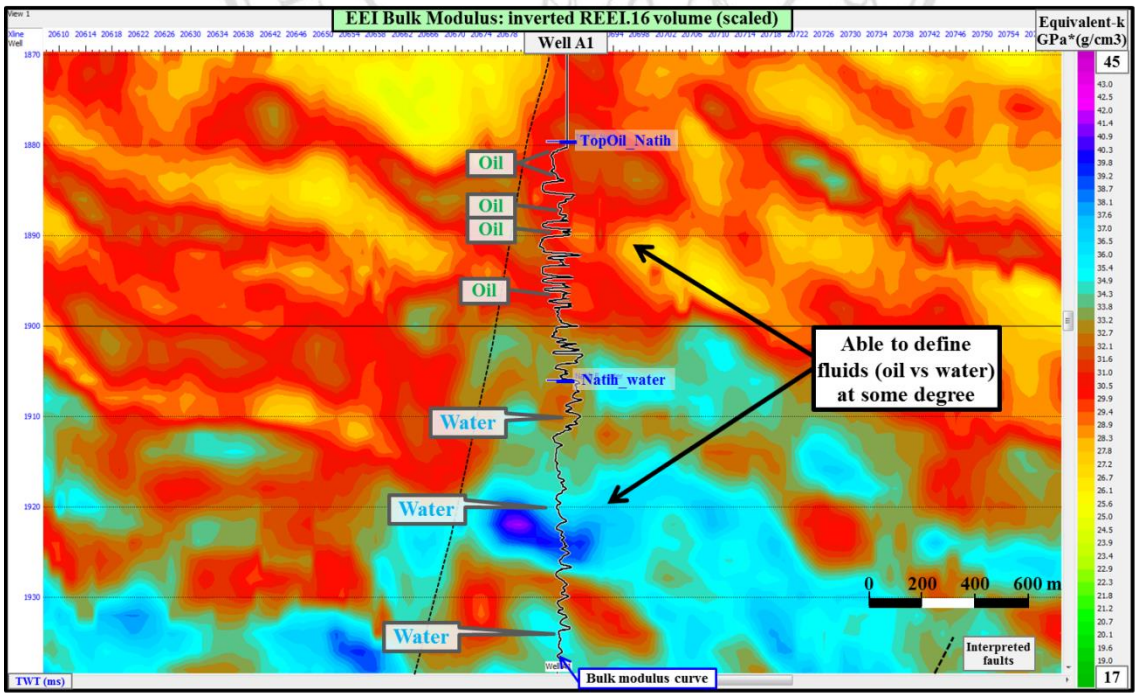

Figure 4.23. The expand view of Figure 4.22 showing the section of inverted-EEI bulk modulus (χ=16°) was well defined the fluid.

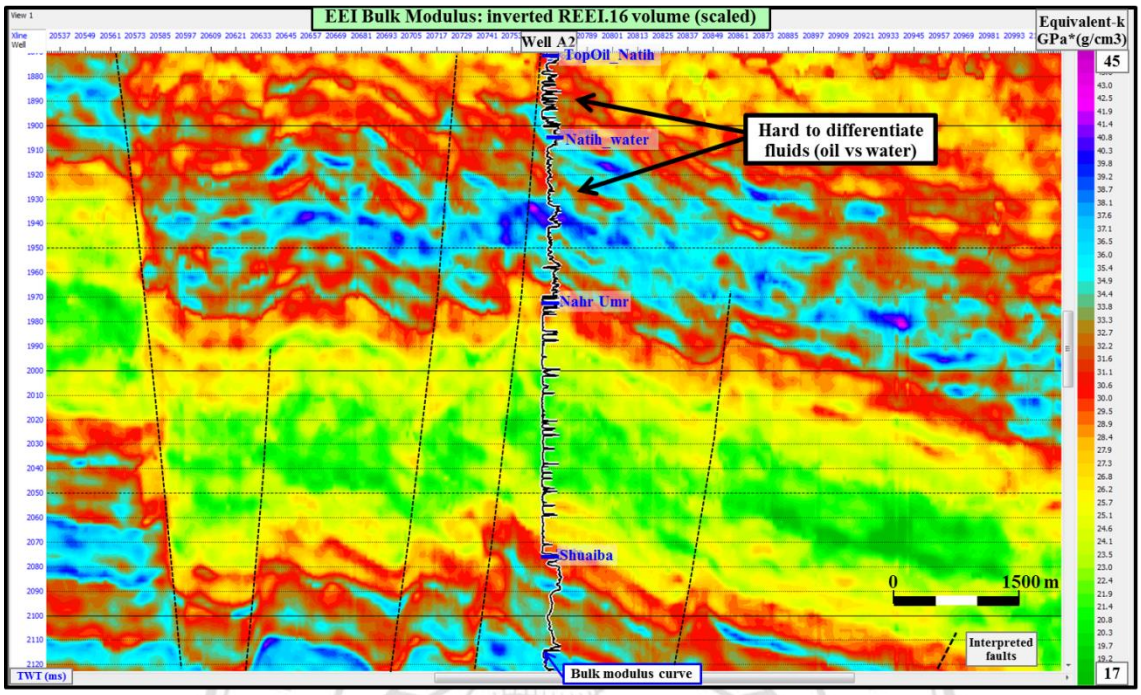

Figure 4.24. The section view of inverted-EEI bulk modulus volume (χ=16°) shows at well A2 with bulk modulus curve. The fluid (oil versus water) and lithology (limestones versus thick-shales interbedded thin-limestone) are well defined.

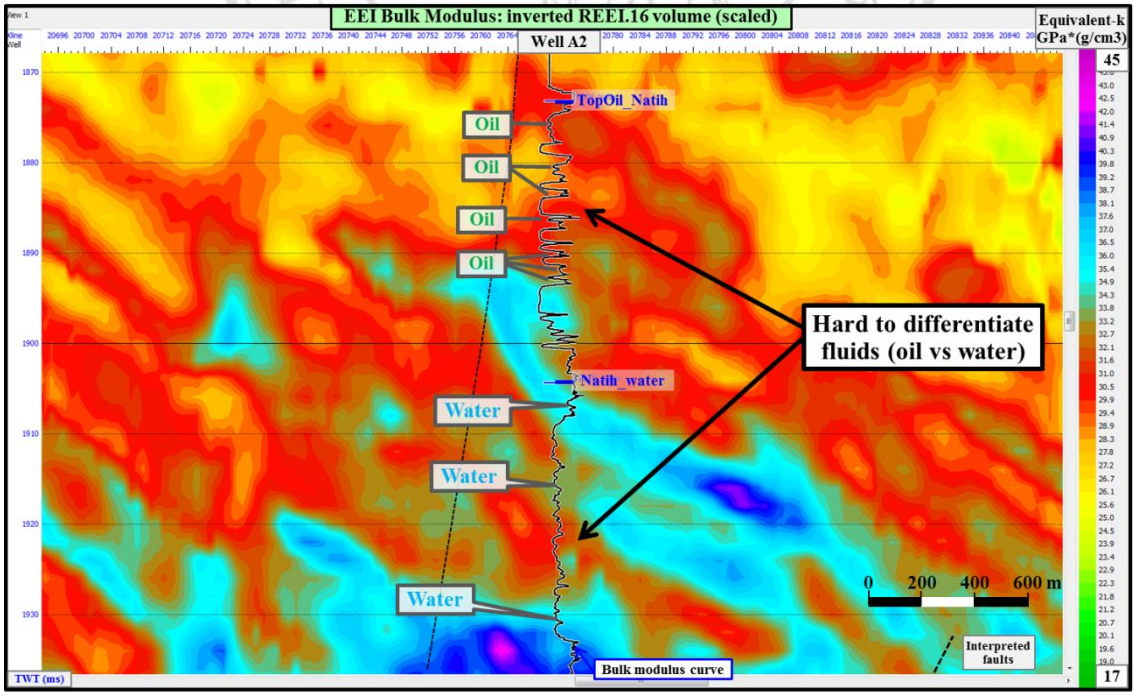

Figure 4.25. The expand view of Figure 4.24 showing the section of inverted-EEI bulk modulus (χ=16°) was well defined the fluid.

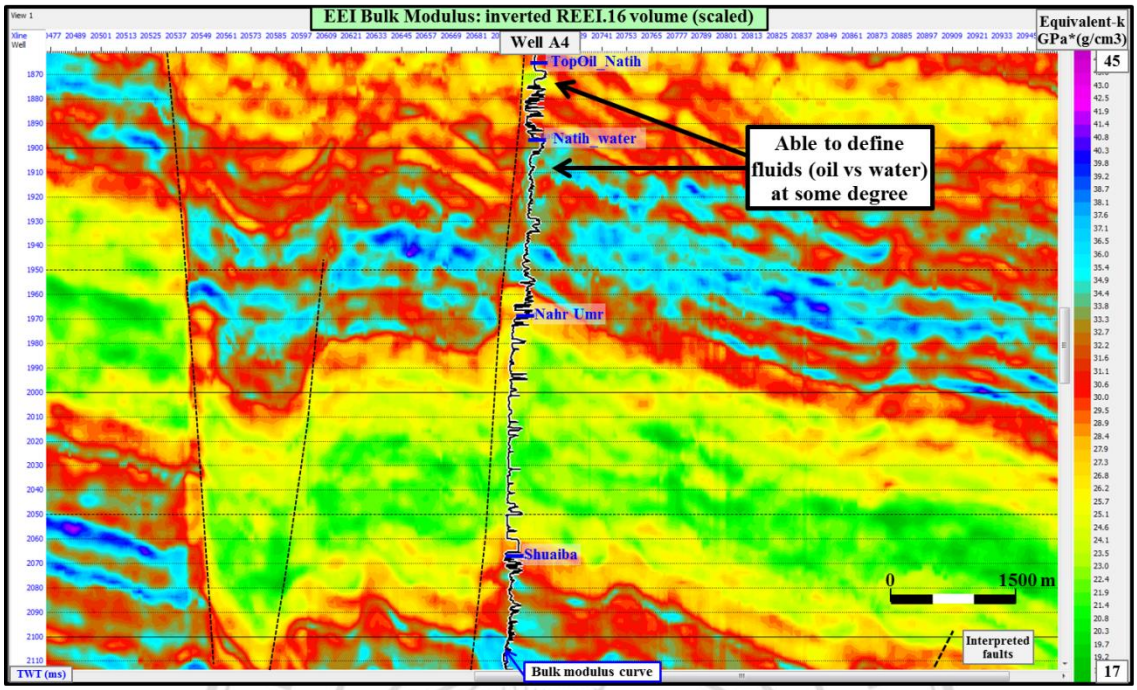

Figure 4.26. The section view of inverted-EEI bulk modulus volume (χ=16°) shows at well A4 with bulk modulus curve. The fluid (oil versus water) and lithology (limestones versus thick-shales interbedded thin-limestone) are well defined.

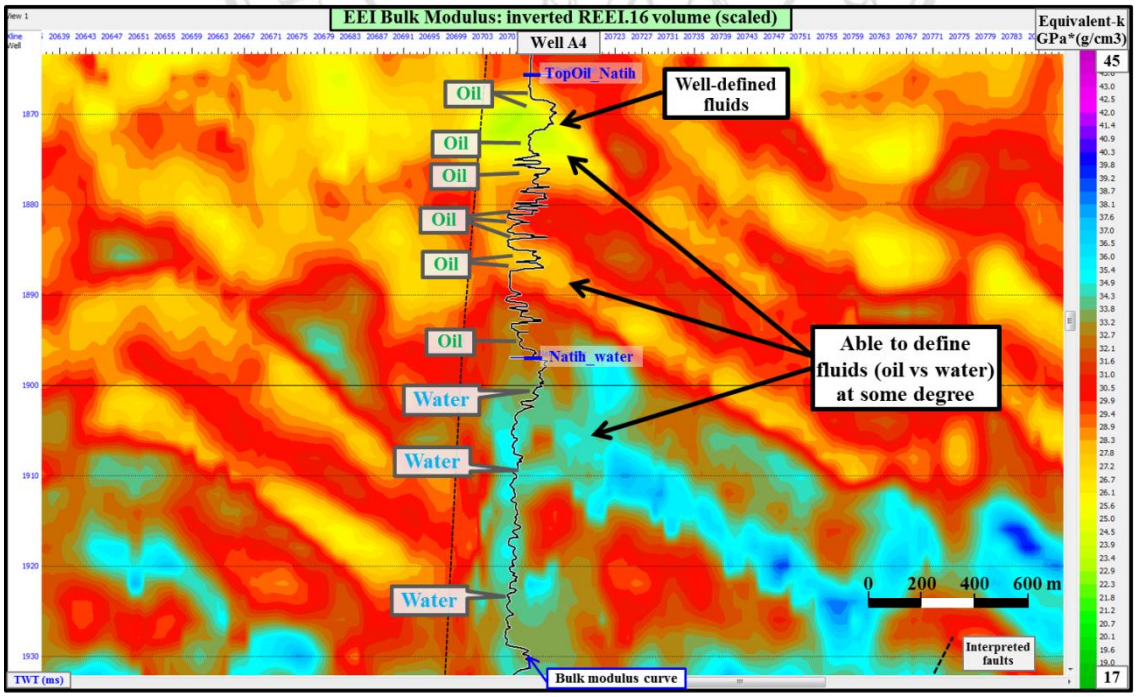

Figure 4.27. The expand view of Figure 4.26 showing the section of inverted-EEI bulk modulus (χ=16°) was well defined the fluid.

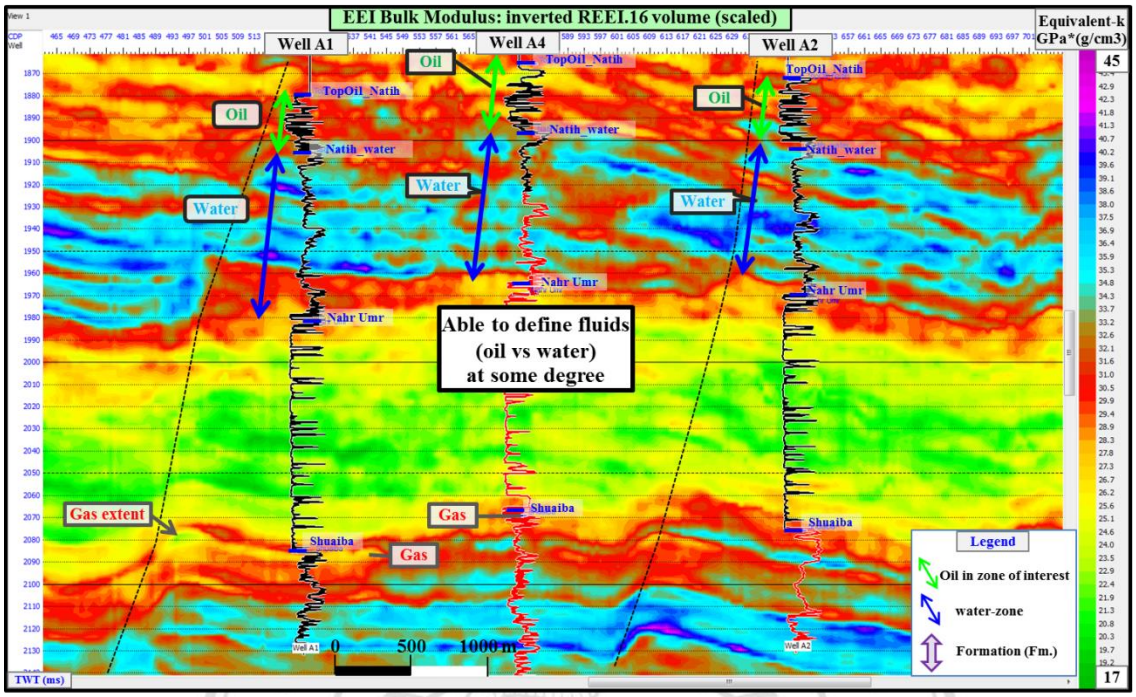

Figure 4.28. The schematic of arbitrary view across well A1, well A4, and well A2 (from left to right) shows the inverted-EEI bulk modulus volume (χ=16°) with bulk modulus logs. The differences in fluid and lithology can be well defined.

4.3.2.2 EEI lambda-rho results

Figure 4.29 shows the section view of the inverted-EEI lambda-rho volume (χ=25°) overlaid by the equivalent log for the well A4 at which the good fit can be seen. From this figure it can be concluded that the result is well defined in both aspects of fluid and lithology. One of oil-bearing reservoirs, that situated at the uppermost of the well log, can be remarkably identified by the low equivalent-EI values (26 - 30 m/s*g/cm^3), which shows the green to yellow color shading pointed by pink arrow. The water-bearing and gas-bearing reservoirs at well A4 were also pointed partly by blue and red arrows respectively (**Figure 4.29**).

As same as the previous results, the limestone sections of Natih and Shuaiba formations can be easily recognized by the common EEI lambda-rho values of more than 33 m/s*g/cm^3 and the main thick-shales interbedded with thin limestones of Nahr Umr formation can be distinguished extraordinarily by the uncommon EI values of less than 33 m/s*g/cm^3.

Figure 4.30 shows the crossline section (20691) across well A2 and well A4 at which there is the identified characteristics of oil-bearing reservoirs in the Natih formation in the uppermost of those wells. Moreover, the similar characteristics of inverted-EEI lambda-rho result can be identified significantly in the same vicinity, here which the extent of oil-bearing reservoirs can be subsequently defined to the left and the right of wells, pointed by pink arrows.

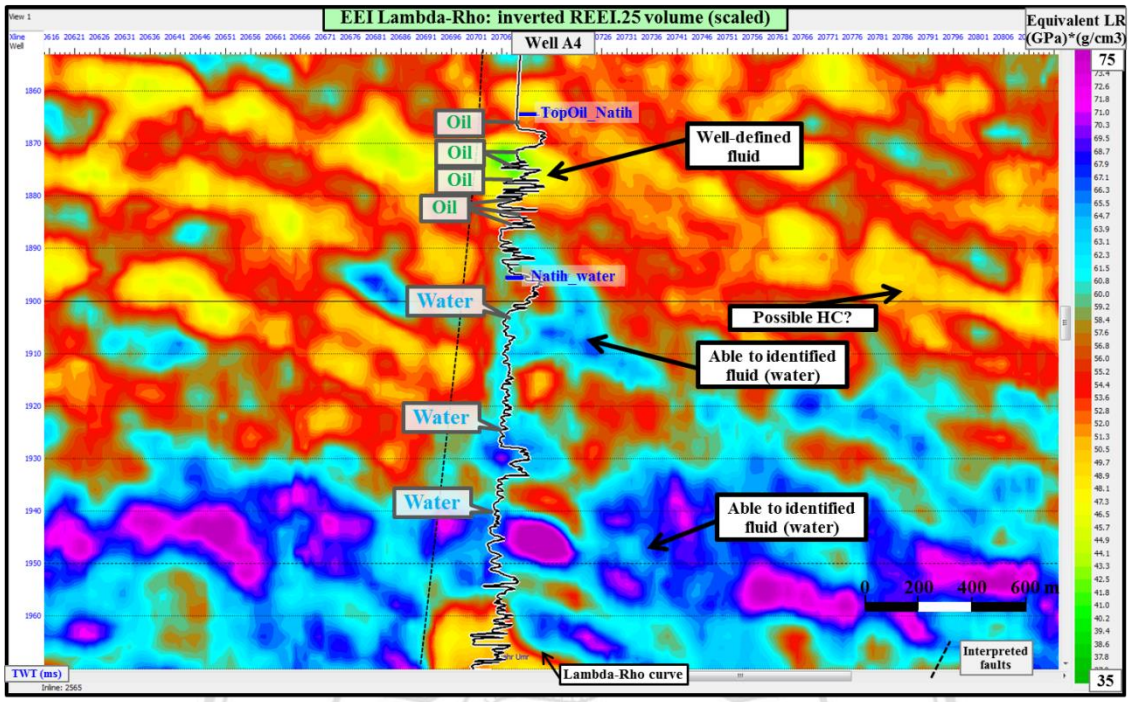

Figure 4.29. The section view of inverted-EEI lambda-rho volume (χ=25°) shows at well A4 with lambda-rho curve. The fluid (oil versus water) is well defined as highlighted.

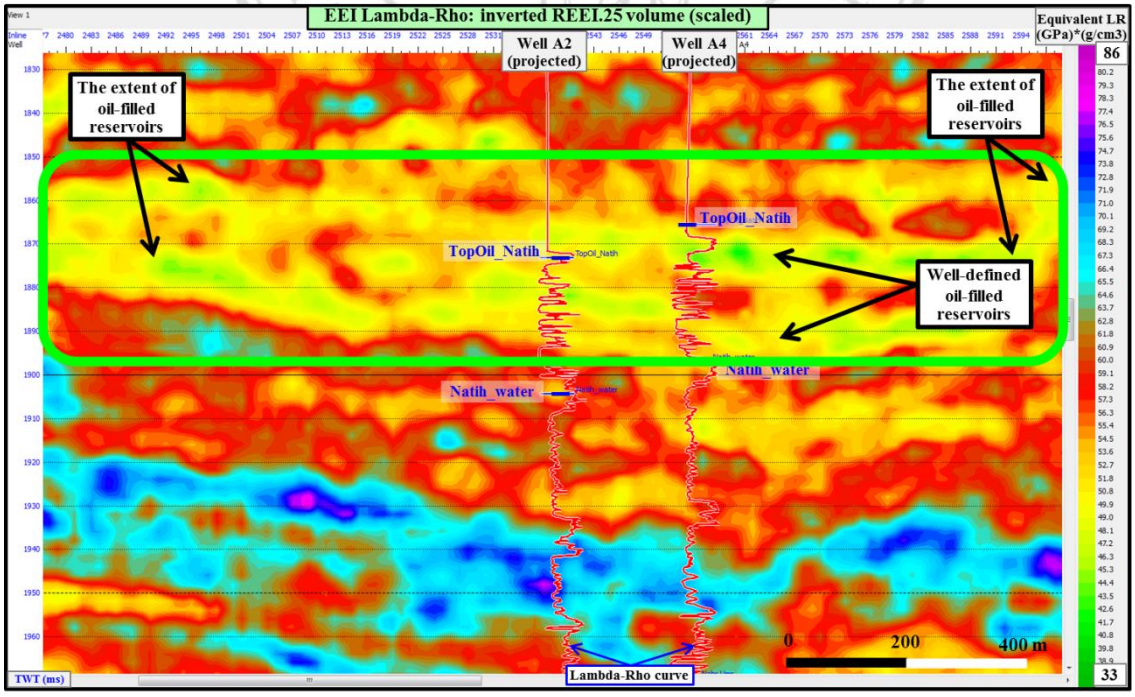

Figure 4.30. The crossline section across well A2 and well A4 shows the identified characteristics and the extents of oil-bearing reservoirs in the Natih formation.

4.3.2.3 EEI mu-rho results

Figure 4.31 shows the section view of the inverted-EEI mu-rho volume (χ= -13°) overlaid by the equivalent log for the well A1 at which the differences in lithology by formation can be well defined, however, in aspect of fluid type cannot identify. From this figure it can be concluded that the result is well differented only in the aspects of lithology.

Nevertheless, the section view of the inverted-EEI mu-rho volume (χ= -13°) overlaid by the equivalent log for the well A4 shows that the uppermost of oil-bearing reservoirs, can be remarkably identified by the low equivalent-EI values (29 - 34 m/s*g/cm^3), which shows the green to yellow color shading (**Figure 4.32**).

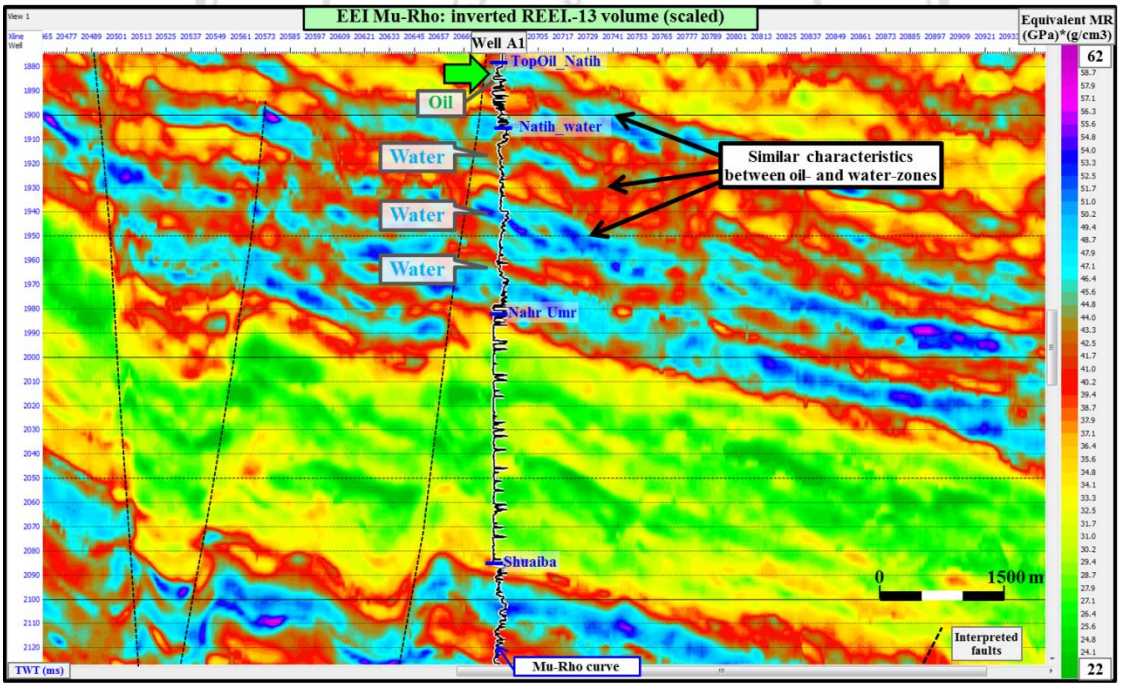

Figure 4.31. The section view of inverted-EEI mu-rho volume (χ= -13°) shows at well A1 with lambda-rho curve. The lithology in the formations of Natih, Nahr Umr, and Shuaiba are well defined, but not for fluid.

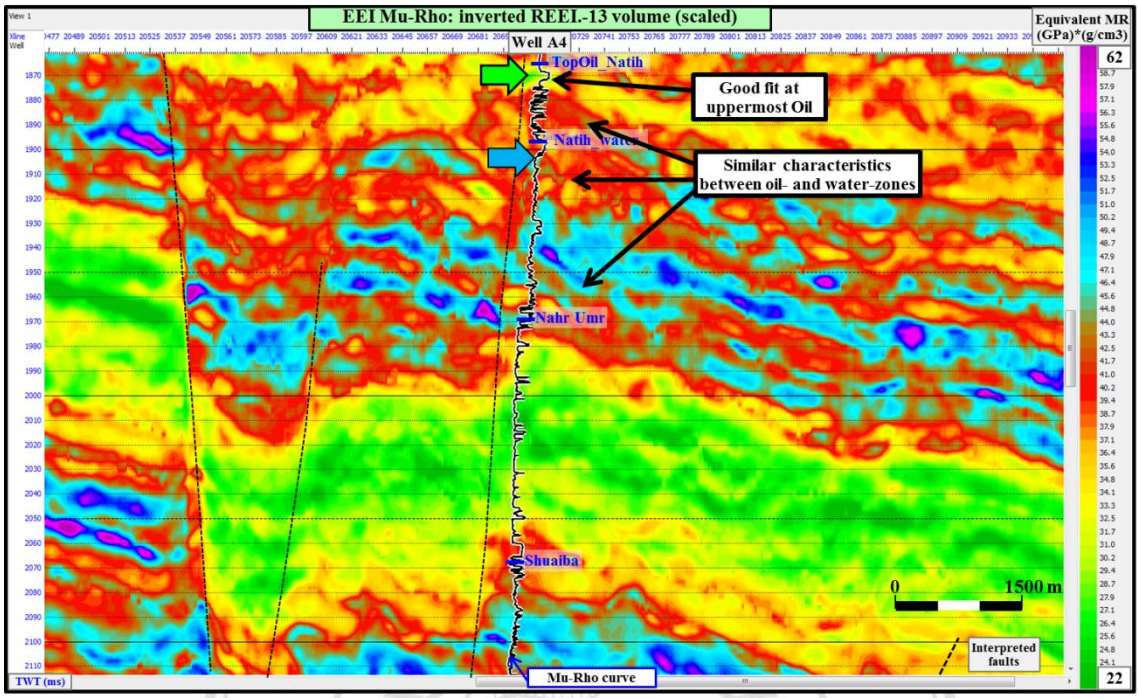

Figure 4.32. The section view of inverted-EEI mu-rho volume (χ= -13°) shows at well A4 with lambda-rho curve. The fluid (oil versus water) is well defined as highlighted.

4.3.2.4 EEI Vp/Vs results

Figure 4.33 shows the section view of the inverted-EEI Vp/Vs volume (χ=38°) overlaid by the equivalent log for the well A4 at which the good fit can be seen in the uppermost of well. The extent of the uppermost oil-bearing reservoir was indicated to the right of well. The fluid is hard to identify because the lower part of oil-bearing zones provides similar characteristics of impedance to the water zone (**Figure 4.33**). From this figure it can be concluded that the result is hard to identify the oil-bearing reservoirs.

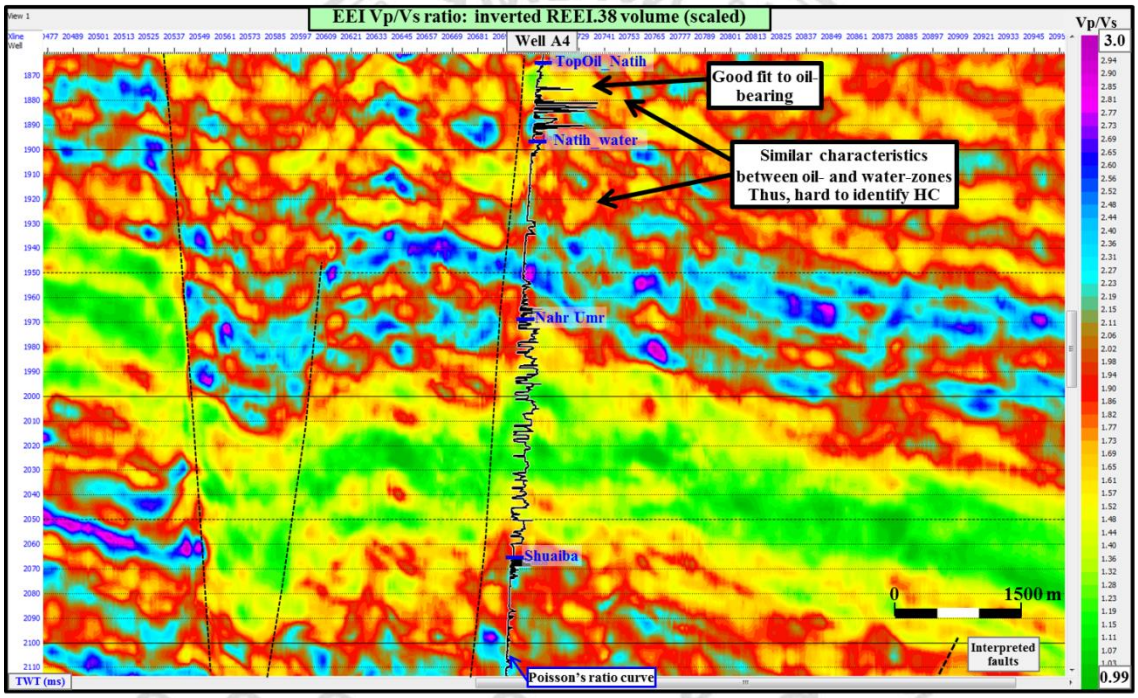

Figure 4.33. The section view of inverted-EEI Vp/Vs volume (χ=38°) shows at well A4 with equivalent curve. The lithology is well defined, but the fluid is partly well defined. The extent of the uppermost oil-bearing reservoir was indicated.

4.3.2.5 Cross-plot of EEI results

From all inverted-EEI results, it can be concluded that the inverted-EEI lambda-rho can characterized very well the oil-bearing reservoirs in the Natih formation. Therefore, this volume would be used to cross-plot with inverted-EEI Vp/Vs to find out other hydrocarbon-bearing reservoirs (**Figure 4.34**).

Firstly, the polygon 1 was created over the cross-plot of EEI lambda-rho versus EEI Vp/Vs to highlight the zone of interest, in this case is the oil-bearing reservoirs in the Natih formation, illustrated in **Figure 4.34**. The cross-section showing the highlighted-green layers correspond to the polygon 1 is illustrated in **Figure 4.35**, here which there is the good fit layer of oil-bearing reservoirs at well A4.

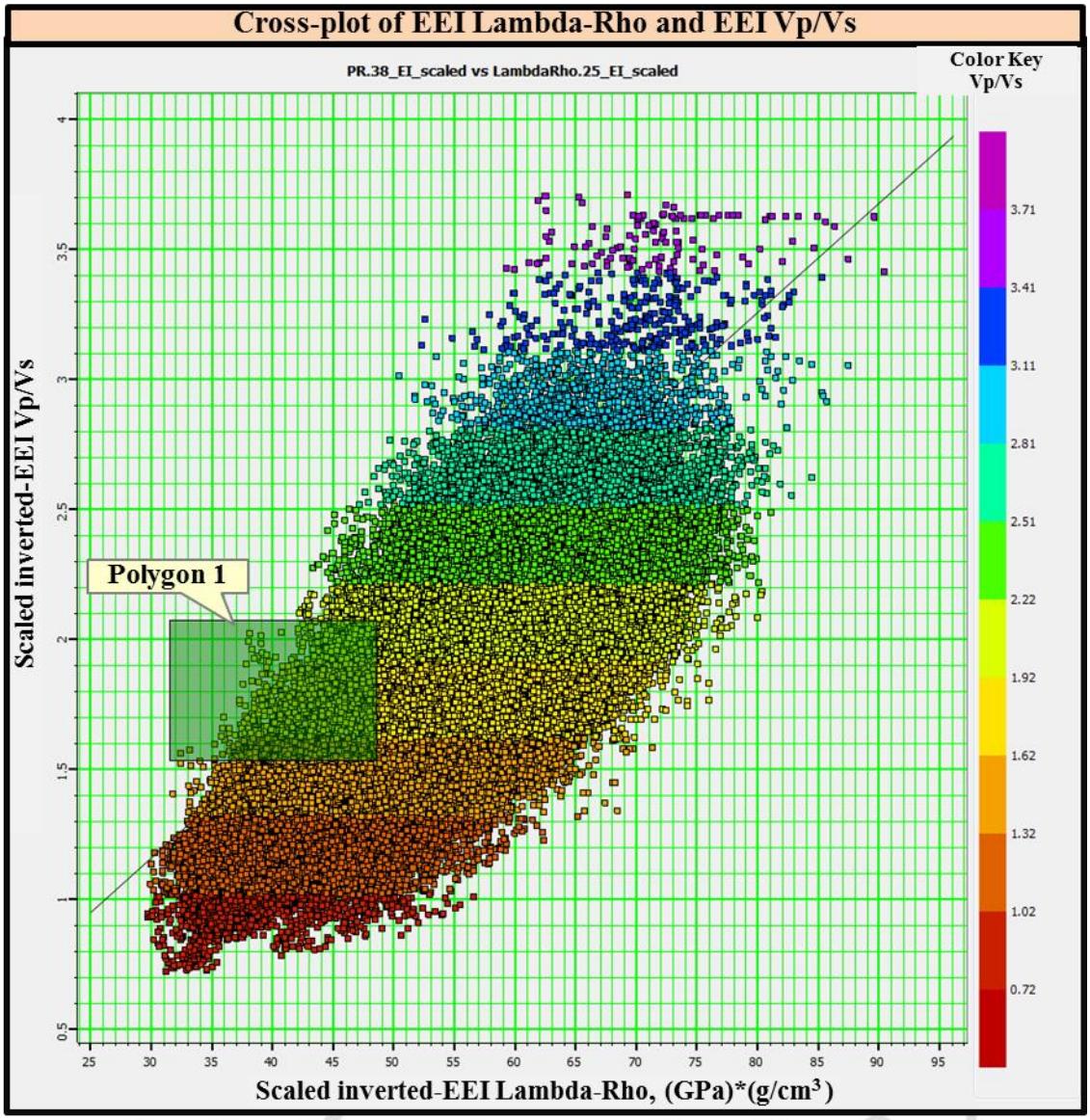

Figure 4.34. Cross-plot between inverted-EEI lambda-rho and inverted-EEI Vp/Vs calculated at the arbitrary line across well A1, A2, and A4 at horizon of Near Natih E with 500 ms of window. The polygon 1 (green polygon) highlighted oil-bearing reservoirs in the Natih Fm.

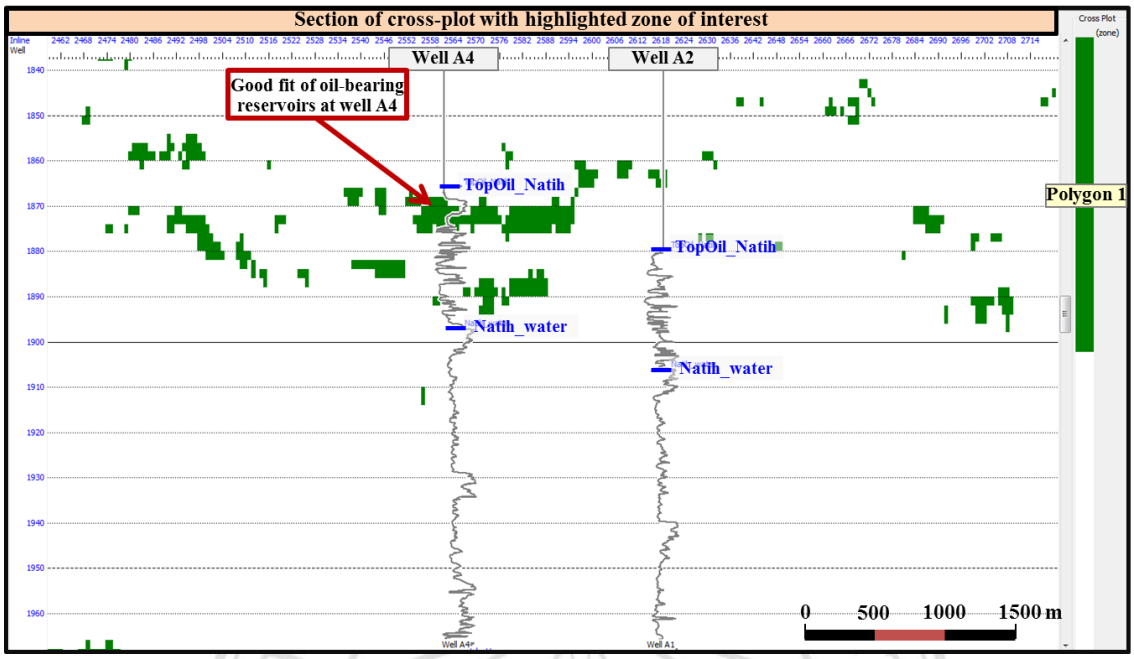

Figure 4.35. The cross-section showing the highlighted-green layers correspond to the polygon 1, here which there is the good fit layer of oil-bearing reservoirs at well A4.reservoirs in the Natih Fm.

Secondly, the polygon 2 was created over the same cross-plot to extend and search for the extents of oil-bearing reservoir in the Natih formation (**Figure 4.36**). After that, the insight section view obtained which shows the green layers corresponding to oil-zones and the above existed-well logs and the extents of oil-zones to both sides of wells (**Figure 4.37**).

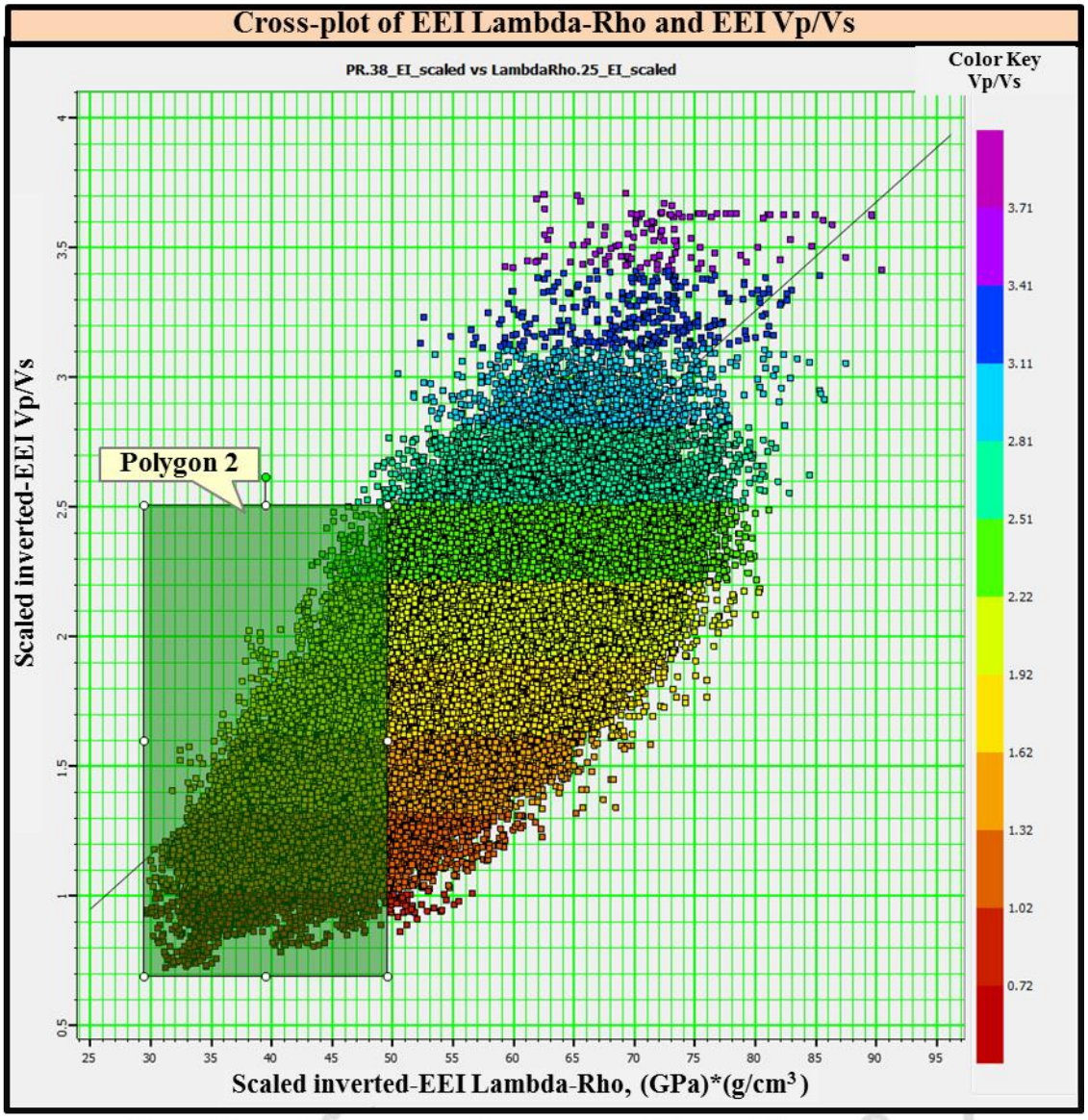

Figure 4.36. Cross-plot between inverted-EEI lambda-rho and inverted-EEI Vp/Vs calculated at the arbitrary line across well A1, A2, and A4 at horizon of Near Natih E with 500 ms of window. The polygon 2 (green polygon) highlighted oil-bearing reservoirs in the Natih Fm.

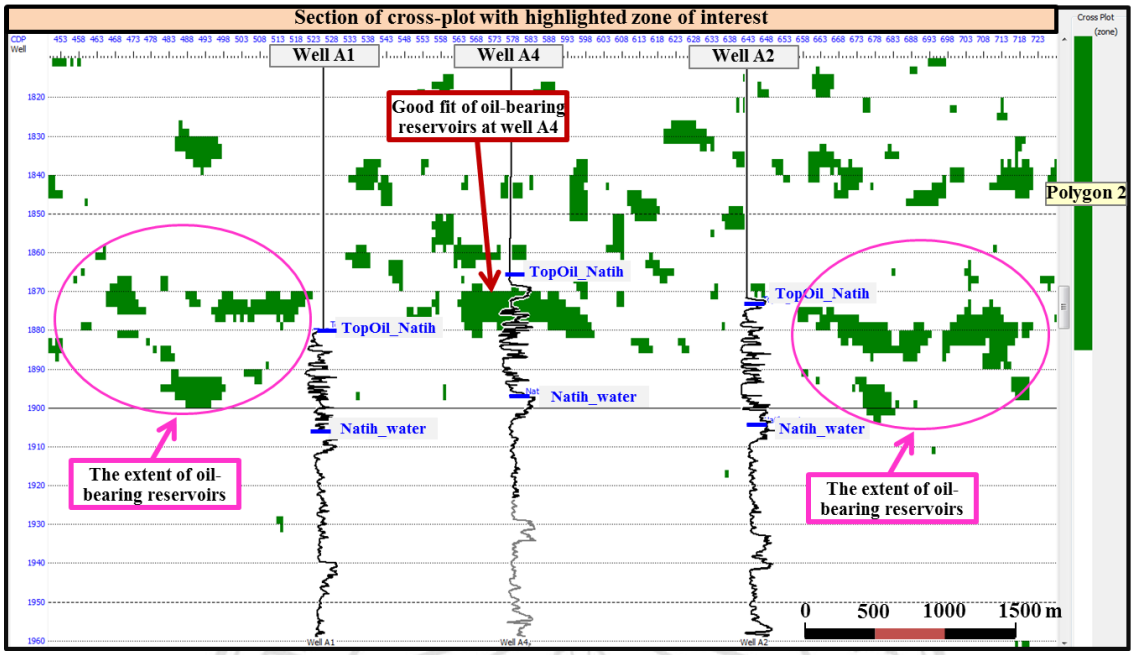

Figure 4.37. The cross-section showing the highlighted-green layers correspond to the polygon 2, here which there is the layers of oil-bearing reservoirs at well A4 and the above existed-well logs and the extents of oil-zones highlighted by pink circles.

Finally, the validity was performed by capturing the same section view of inverted-EEI lambda-rho volume and adjusting the scale to highlight the oil-bearing reservoirs found in well A1, well A2, and well A4. **Figure 4.38** shows the comparison between the cross-section with highlighted-green layers of oil zones (A) and the section of scaled-EEI lambda-rho with well-characterized oil zones, at which the same oil-bearing extents to both sides can be seen highlighting by pink circles in (A) and by black circles in (B).

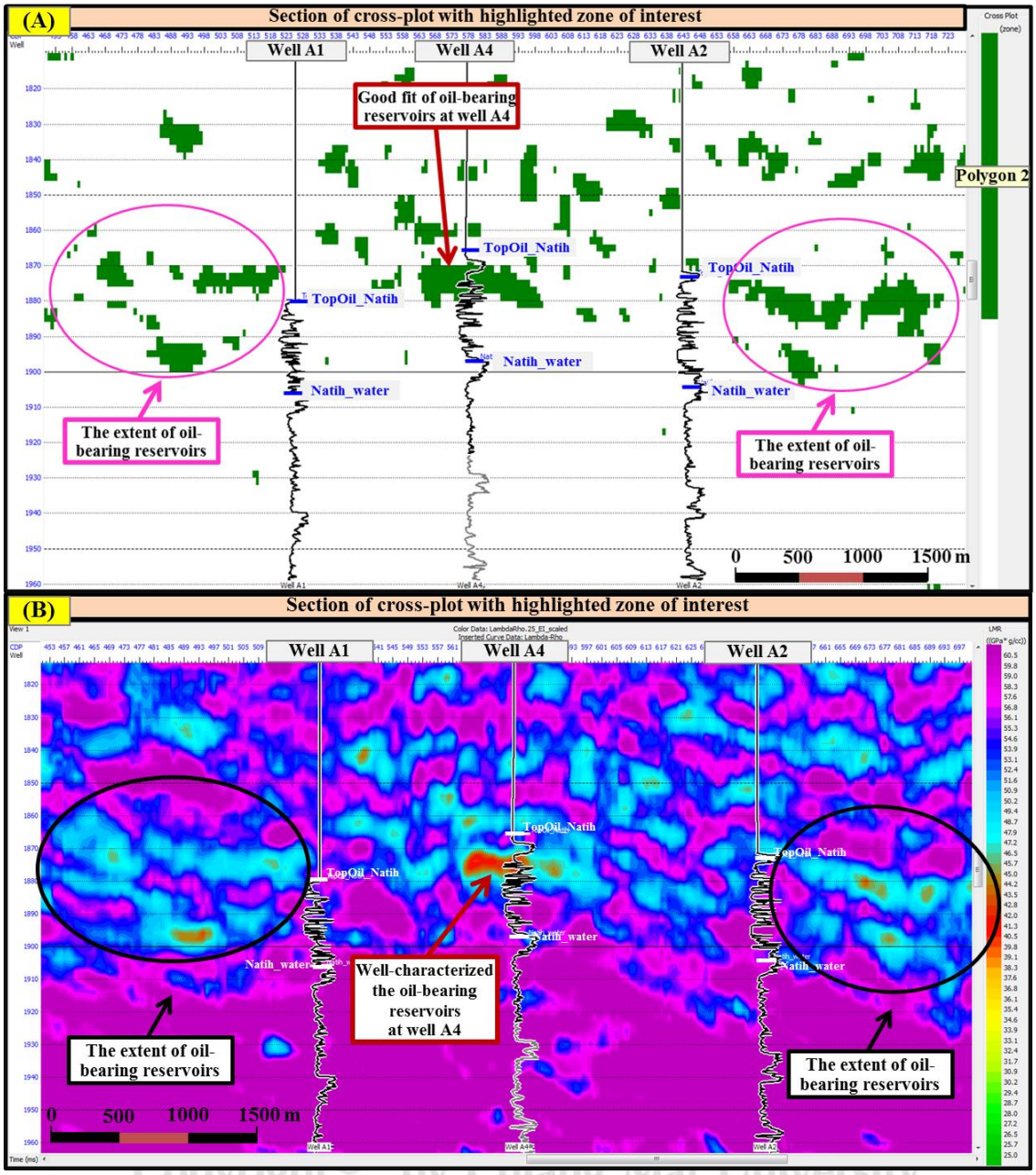

Figure 4.38. Two section views compared the highlighted-green layers of (A) and the EEI lambda-rho characteristics of (B), at which the same oil-bearing extents to both sides can be seen highlighting by pink circles in (A) and by black circles in (B).

4.3.2.6 Horizon slices and blind well test

To visualize the lateral extension in the map view, the horizon slices of EEI lambda-rho volume were conducted in different window extraction, and then the selected parameters of shifted 10 ms up and window length of 50 ms shows the best result (**Figure 4.39 – 4.40**), hence this setting will be used for other volumes. **Figure 4.39** shows the horizon slice extracted from EEI lambda-rho volume which horizon of near base Fiqa shifted -10 ms (going up) with 50 ms of centered target window and blue rectangle highlighted the zoom view of its (**Figure 4.40**).

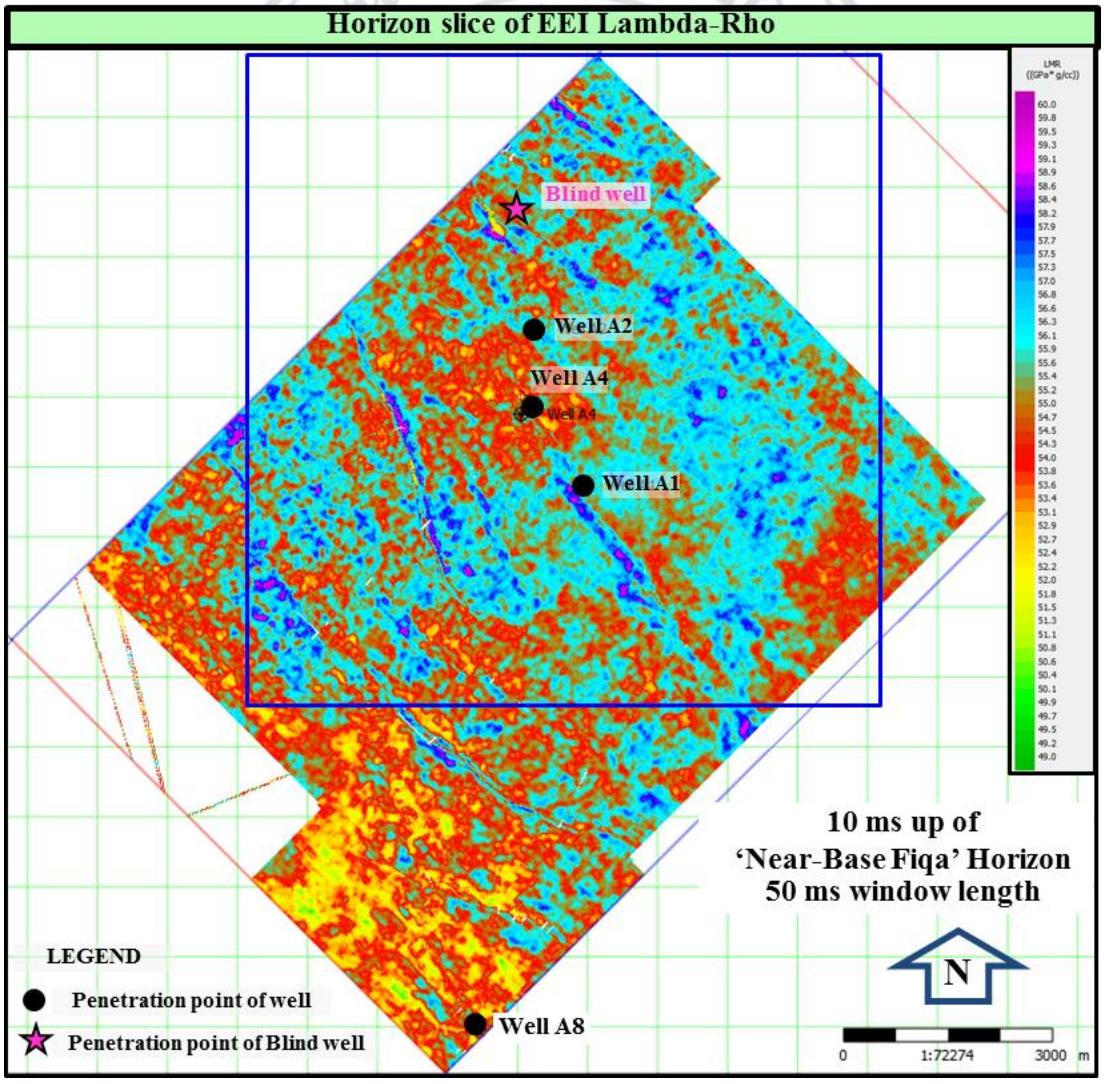

Figure 4.39. Horizon slice of shifted 10 ms up of Near Base Fiqa extracted from EEI lambda-rho volume with centered 50 ms window length. The wells in this study were depicted.

The blind well, that is the well not incorporated in the initial model and EEI analyses, was introduced here to test the EEI inversion results and it was posted over those horizon slices locating to the north of well A2 in the following figures.

In **Figure 4.40**, the X-X' line (white line) and the highlighted-extent of anomaly spotted at well A4 (black dotted-free form) were depicted. From this figure the clear interpretation could be made which at first, the oil-bearing reservoirs at well A4 matched to EEI lambda-rho anomaly, then this anomaly was highlighted by black dotted-free form, secondly the result matched with hydrocarbon-bearing reservoirs at blind well. The thickness of hydrocarbon-bearing reservoirs, either oil or gas, at each well was indicated in the bracket (**Figure 4.40**).

However, this result also shows as inconclusive interpretation because it is unable to highlight the oil-bearing reservoir proven at well A1 and well A2 and also no well calibration at surrounding anomalous-color locations pointed by question marks (**Figure 4.40**). One possible explanation might be that the EEI result would be promising if the hydrocarbon-bearing reservoirs were thick enough.

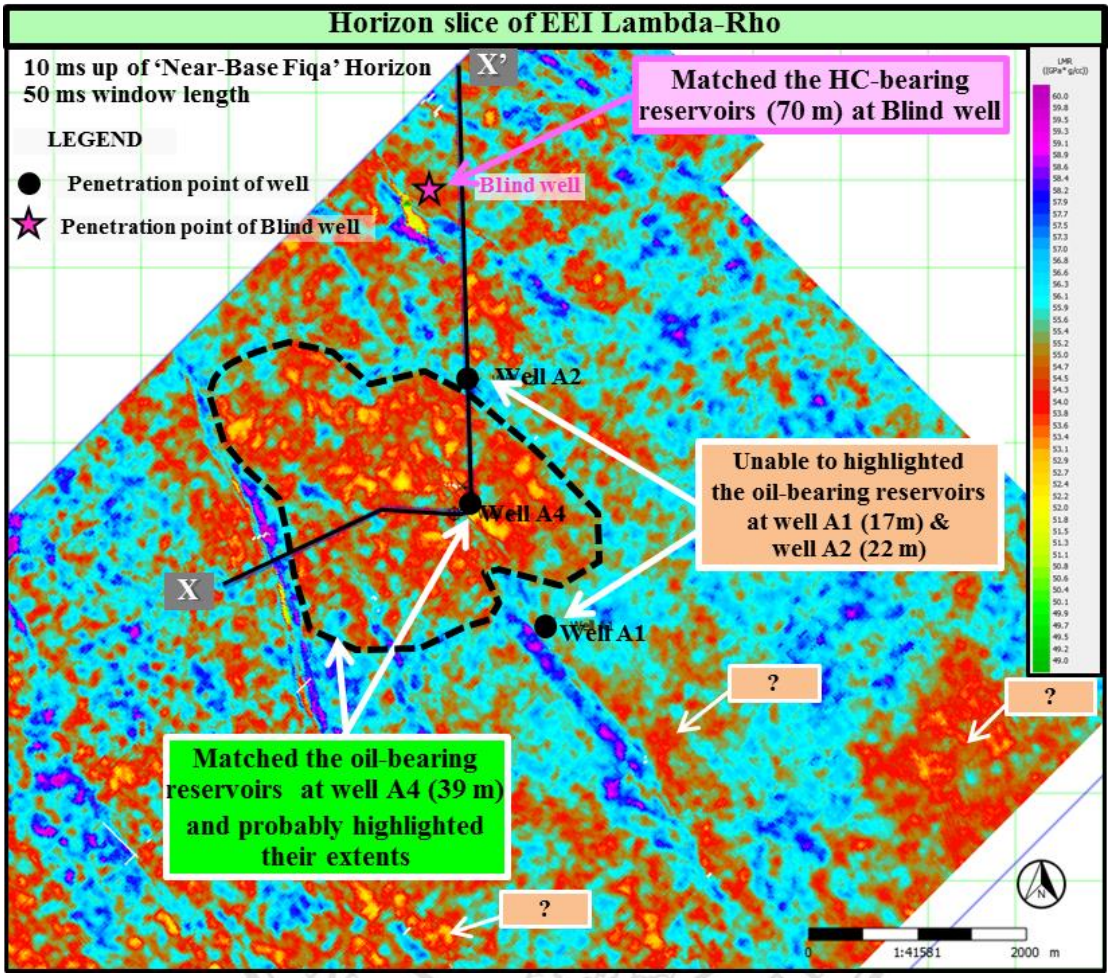

Figure 4.40. The zoom view of EEI lambda-rho horizon slice along horizon of near base Fiqa depicted the X-X' line, the highlighted-extent of anomaly spotted at well A4, good matching at blind well and some inconclusive interpretations.

The section of X-X' line can be seen in **Figure 4.41**, at which horizon of near base Fiqa, well A4 and well A2 with their lambda-rho logs were posted. The black-double arrows were indicated the window extraction of that horizon slice that is about 50 ms length with shifting up 10 ms of horizon near base Fiqa as centered.

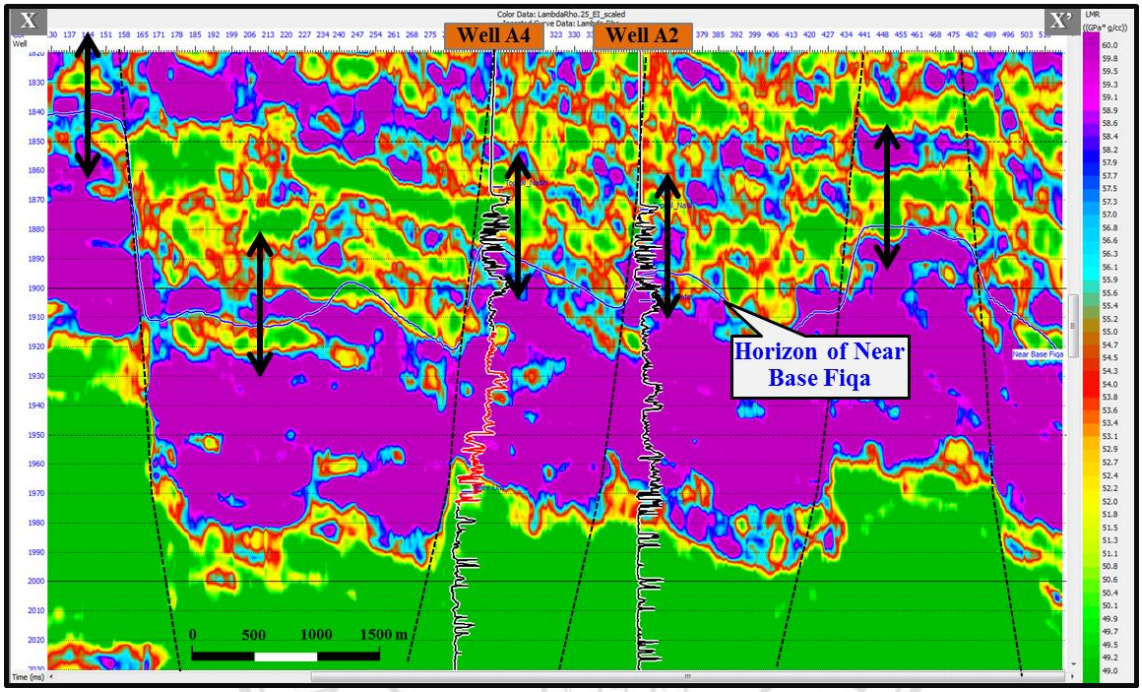

Figure 4.41. The scaled-EEI lambda-rho section of X-X' line across the highlighted-extent of anomaly spotted at well A4 shows the corresponding that anomaly in which the black-double arrows indicated the window extraction of that horizon slice.

Although, that horizon slice of EEI lambda-rho is not perfectly for fluid identification as study's objective, however, the attempts of result evaluations have still been continued. Thus, other horizon slices would be discussed in the following. The horizon slice of Near Natih E horizon extracted from volume difference between EEI lambda-rho and EEI Vp/Vs was generated to reveal some anomalies, and then (**Figure 4.42**) its result illustrated some sweet spots locating at all hydrocarbon well locations (well A1, A2, A4, & blind well) and surroundings. **Figure 4.42** illustrated that the sweet spots provide evidently the clues implying the regions of hydrocarbon accumulations in this zone of interest which is worthily for prospect evaluation.

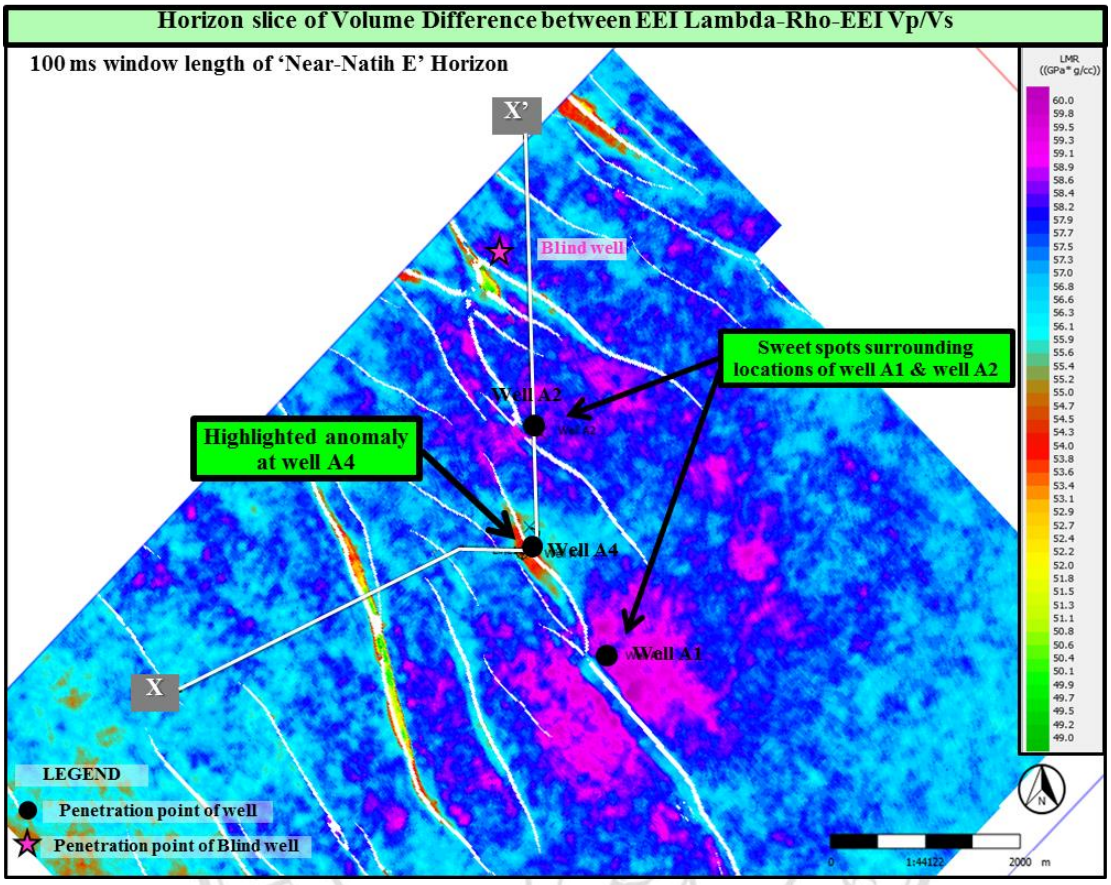

Figure 4.42. Horizon slice of Near Natih E extracted from volume difference between EEI lambda-rho and EEI Vp/Vs with 100 ms window length. The sweet spots at wells, blind well and surroundings were depicted.

Figure 4.43 shows horizon slice of EEI bulk modulus volume with shifted 10 ms up and centered 50 ms window length of near base Fiqa horizon. From this figure, although not all hydrocarbon wells matched to EEI bulk modulus result, but this horizon slice could provide some clue implying the different between regions of hydrocarbon and non-hydrocarbon. To the south of well A1, the unknown anomalies were pointed by question marks (**Figure 4.43**) due to the weakness of fluid identification.

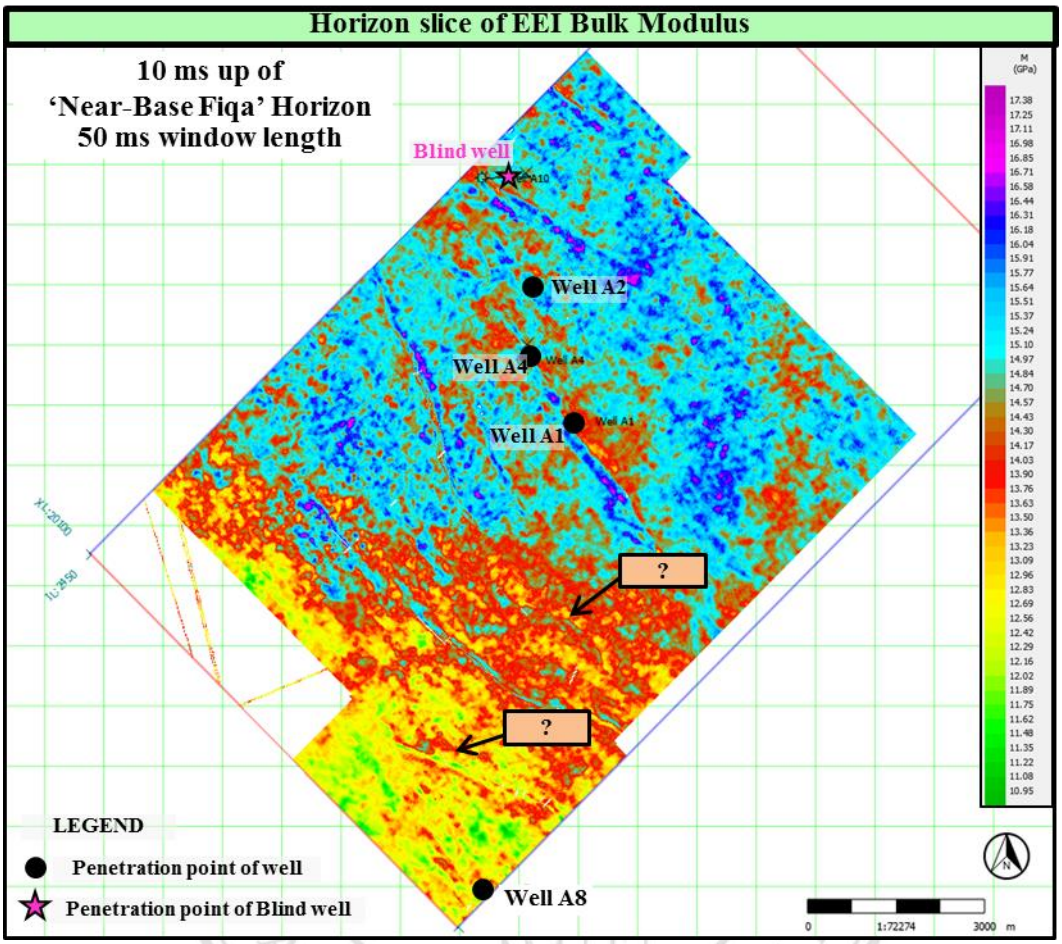

Figure 4.43. Horizon slice of shifted 10 ms up of Near Base Fiqa extracted from EEI bulk modulus volume with centered 50 ms window length.

Figure 4.44 shows horizon slice of EEI shear modulus volume with the same setting extraction from near base Fiqa horizon. From this figure it could not provide perfectly the conclusive fluid identification, not matched at well A1 and A2, but the challenging sweet spots conformed the structure were depicted for prospective consideration. The important thing is this horizon slice of EEI shear modulus illustrating good fit at blind well (**Figure 4.44**).

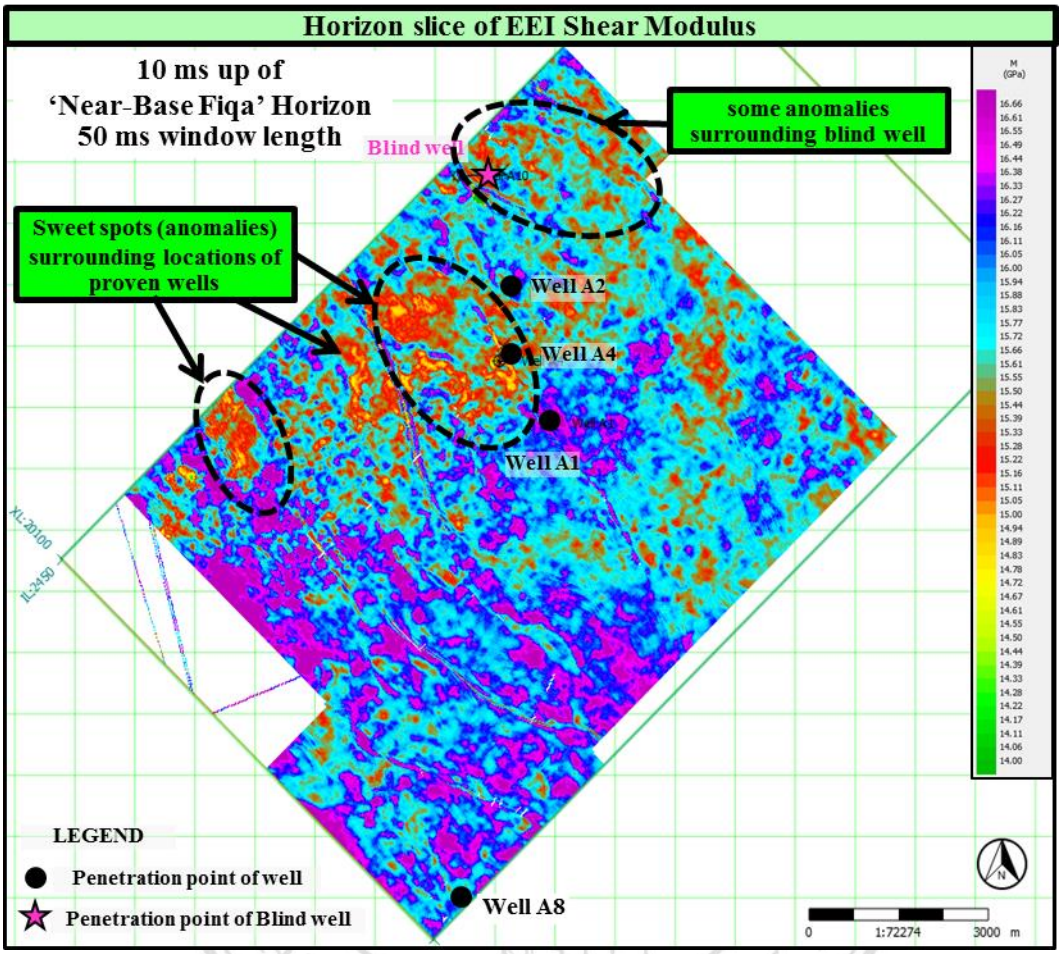

Figure 4.44. Horizon slice of shifted 10 ms up of Near Base Fiqa extracted from EEI shear modulus volume with centered 50 ms window length. The black dotted-ovals highlighted the sweet spots.

Figure 4.45 shows horizon slice of EEI Mu-Rho volume with the same setting parameter as previous for near base Fiqa horizon at which the good matching at well A4 and blind well and the highlighted sweet spots can be seen. There are 2 zoomed views showing the EEI mu-rho horizon slice significantly matched with those wells, and also the indicated prospective area could be probably the drilling candidate.

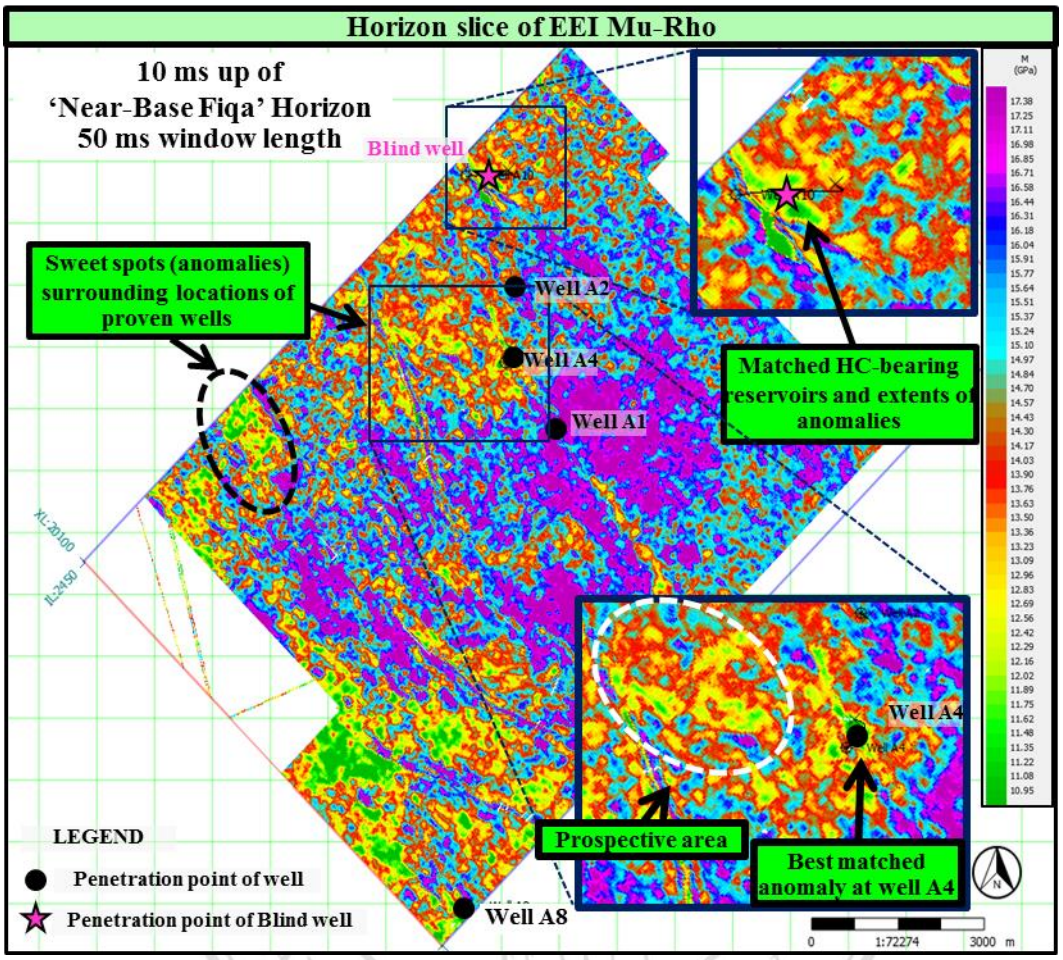

Figure 4.45. Horizon slice of shifted 10 ms up of Near Base Fiqa extracted from EEI Mu-Rho volume with centered 50 ms window length.

Figure 4.46 shows horizon slice of EEI Vp/Vs volume with the same setting as previous from near base Fiqa horizon. From this figure, there are good matches of oil-bearing reservoirs at well A2 and A4 and good match of water-bearing reservoir at well A8 (**Figure 4.46**). However, it still could not provide any good interpretation due to the weakness of fluid identification and unknown anomalies.

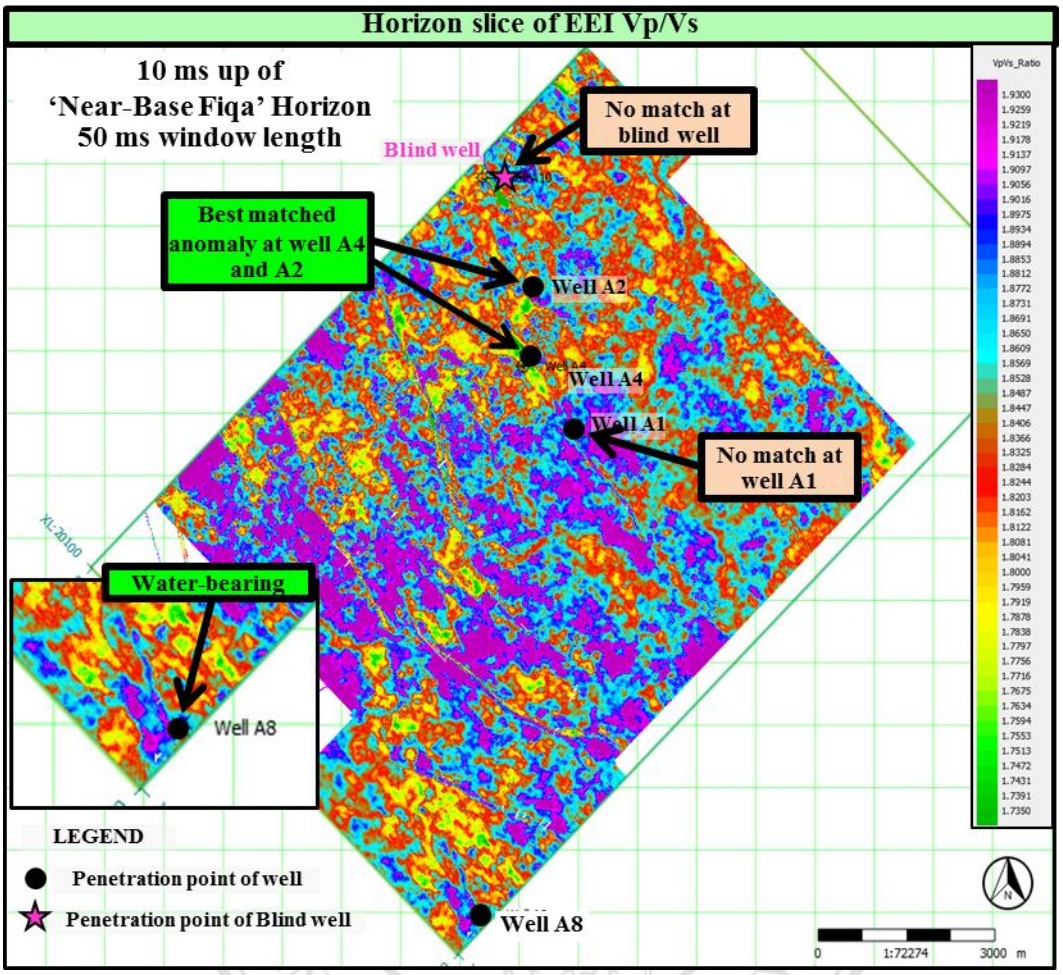

Figure 4.46. Horizon slice of shifted 10 ms up of Near Base Fiqa extracted from EEI Vp/Vs volume with centered 50 ms window length.